

ER–mitochondria contacts orchestrate mitochondrial transport via C19orf12/EMTRAS

**Xiayuhe Pei^{1,*}, Shuqian Zhang^{2,*}, Peiyang Li³, Yutong Wu¹, Yiru Cheng¹, Xia Feng^{4,5}, Yiqian Wu³,
Xiaoshuai Huang⁶, Ning Huang^{7,8}, Bei Liu³, Junlin Teng¹, Jianguo Chen^{1,9,#}, Craig Blackstone^{4,5,#}, Pengli
Zheng^{1,2,10,#}**

¹Key Laboratory of Cell Proliferation and Differentiation of the Ministry of Education, State Key Laboratory of Membrane Biology, School of Life Sciences, Peking University, Beijing 100871, China

²Peking-Tsinghua Center for Life Sciences, Academy for Advanced Interdisciplinary Studies, Peking University, Beijing 100871, China

³National Biomedical Imaging Center, College of Future Technology, Peking University, Beijing 100871, China

⁴MassGeneral Institute for Neurodegenerative Disease, Massachusetts General Hospital, Charlestown, MA 02114, USA

⁵Department of Neurology, Massachusetts General Hospital and Harvard Medical School, Boston, MA 02114, USA

⁶Beijing Advanced Center of Cellular Homeostasis and Aging-Related Diseases, Institute of Advanced Clinical Medicine, Peking University, Beijing, 100191, China.

⁷Institute of Neuroscience, Translational Medicine Institute, Health Science Center, Xi'an Jiaotong University, Xi'an 710061, China

⁸Department of Physiology and Pathophysiology, School of Basic Medical Sciences, Health Science Center, Xi'an Jiaotong University, Xi'an 710061, China

⁹Center for Quantitative Biology, Academy for Advanced Interdisciplinary Studies, Peking University, Beijing 100871, China

¹⁰Lead contact

* These authors contributed equally to this work.

Correspondences:

Jianguo Chen: chenjg@pku.edu.cn

Craig Blackstone: cblackstone@mgh.harvard.edu

30 Pengli Zheng: zhengpl@pku.edu.cn

31

32 **Abstract**

33 Endoplasmic reticulum (ER)–mitochondria contact sites facilitate lipid transfer, calcium signaling, and
34 mitochondrial division, yet their role in mitochondrial transport remains unclear. Here, we identify Hereditary
35 spastic paraplegia (HSP)-associated protein C19orf12 as an ER-anchored protein that acts as a central
36 organizer for mitochondrial trafficking and rename it EMTRAS (ER–anchored Mitochondrial Trafficking
37 Scaffold). Loss of EMTRAS leads to severe perinuclear mitochondrial clustering in cells, impaired anterograde
38 transport in neurons, and progressive locomotor dysfunction in mice that recapitulates key features of HSP.
39 Mechanistically, EMTRAS forms a discrete complex with the mitochondrial Rho GTPase Miro1 and the
40 kinesin-1 motor Kif5b, independently of the canonical TRAK adaptors, thereby directly linking ER–
41 mitochondria contact sites to microtubule-based anterograde transport. This interaction is dynamically
42 regulated by local calcium levels: enhanced at Ca^{2+} concentrations (1–10 μM) characteristic of ER–
43 mitochondria contact microdomains, coinciding with increased mitochondrial motility, but markedly
44 suppressed under high calcium conditions, correlating with mitochondrial transport arrest. Therefore, our
45 findings establishes ER-mitochondria contact sites as logistical hubs for Kinesin-1 motor loading and
46 highlights the importance of the calcium-tunable EMTRAS scaffold in sustaining directional mitochondrial
47 transport, revealing how the loss of this regulation drives the neurodegenerative cascade.

48

49 Key words: ER–mitochondria contact sites; Mitochondrial transport; C19orf12/EMTRAS; Miro1; Kif5b;
50 Hereditary Spastic Paraplegia

51

52 Introduction

53 Cells continuously adjust the dynamic distribution of their organelles through intracellular transport to ensure
54 the efficient and orderly execution of cellular activities. Among these, mitochondria are essential metabolic
55 hubs that participate in key cellular processes such as ATP production, calcium buffering, and apoptosis¹⁻³.
56 Mitochondrial transport is critical for cells to maintain spatial energetic and metabolic balance, and is
57 particularly indispensable for highly specialized cells with extended morphologies and intense energy demands,
58 most notably neurons²⁻⁵. Neurons possess elongated axons and rely on precise mitochondrial delivery to distal
59 synapses to sustain synaptic transmission, plasticity, and survival. Consequently, aberrant mitochondrial
60 transport is a hallmark of numerous neurodegenerative disorders, including Alzheimer's disease, Parkinson's
61 disease, inherited neuropathies, and Hereditary spastic paraplegia (HSP)⁶⁻⁸.

62 Mitochondrial trafficking is driven by a diverse repertoire of molecular motors and adaptors. Long-range
63 anterograde transport is primarily mediated by microtubule-based kinesin-1 (Kif5) and kinesin-3 (Kif1b)⁹,
64 while retrograde movement relies on cytoplasmic dynein^{10,11}. Beyond these long-range transporters, short-
65 range motility in actin-rich domains utilizes Myosin19^{12,13}. These motors are coupled to the mitochondrial
66 surface via adaptor complexes, including the Metaxins¹⁴ and, most notably, the mitochondrial Rho GTPases
67 (Miro1/2)^{15,16} and trafficking kinesin-binding proteins (TRAK1/2)¹⁷⁻²⁰. A fundamental question thus arises:
68 how does the cell spatially coordinate these ubiquitous motors and adaptors to ensure mitochondria are
69 mobilized or anchored at the right time and place?

70 A critical regulatory feature of this machinery centers on Miro1, which harbors EF-hand motifs to sense
71 cytosolic Ca²⁺ (cCa²⁺). Specifically, a sharp increase in local cCa²⁺—such as that occurring during neuronal
72 depolarization or synaptic activity—acts as a well-recognized “stop signal” that inhibits mitochondrial
73 movement, particularly in neurons^{21,22}. While this arrest is believed to involve Ca²⁺-induced conformational
74 changes in Miro1, the exact molecular basis for motor inhibition remains incompletely understood, as studies
75 have proposed either the decoupling of kinesin from its cargo or the direct impediment of motor–microtubule
76 attachment. Additionally, this process is further modulated by interactions with the mitochondrial calcium
77 uniporter (MCU) and mitochondrial matrix calcium dynamics^{23,24}. Importantly, distinct from these inhibitory
78 mechanisms, the role of basal physiological Ca²⁺ levels remains less defined, although emerging evidence
79 suggests that specific calcium concentrations may be required for the integrity of the mitochondrial transport
80 complex, rather than solely acting as a stop signal²⁴⁻²⁷.

81 As the largest membranous organelle in the cell, the endoplasmic reticulum (ER) functions as a central
82 platform for organelle communication²⁸. Through extensive membrane contact sites (MCSs), the ER
83 orchestrates essential physiological processes, including calcium transfer²⁹, lipid exchange³⁰, and
84 mitochondrial fission–fusion dynamics^{31,32}. Previous work from our laboratory has demonstrated that the
85 structural distribution of the ER broadly dictates the spatial organization of almost all other membrane-bound
86 organelles³³. This suggests that the ER may play a central, yet underappreciated, role in governing broad
87 organelle transport. Supporting this idea, specific ER-resident proteins are already known to actively regulate
88 the transport of endosomes and lysosomes: for instance, Protrudin acts as a scaffold that simultaneously binds

89 Kinesin-1 and the endosomal protein Rab7, thereby promoting the anterograde transport of late endosomes
90 and lysosomes³⁴. For mitochondria, recent studies have further suggested that ER tubules can mechanically
91 guide mitochondrial positioning via “hitchhiking” mechanisms³⁵—and notably, the mitochondrial transport
92 regulator Miro1 is enriched at ER–mitochondria interface³⁶. Together, these observations hint that ER-
93 resident proteins may actively regulate mitochondrial motility, yet whether such ER proteins directly recruit
94 or modulate the mitochondrial transport machinery itself remains unknown.

95 HSP provides a compelling genetic window into this potential ER-transport link. HSP is characterized by
96 the length-dependent degeneration of corticospinal motor neurons, leading to progressive lower limb
97 spasticity³⁷. Strikingly, over 60% of pathogenic HSP mutations occur in ER-shaping or ER-resident proteins
98 (e.g., Atlastins, REEPs, Spastin³⁷), implicating ER dysfunction as a primary driver of axonopathy. Yet, the
99 downstream consequence of these ER mutations often manifests as defects in axonal transport and
100 mitochondrial distribution³⁸. This disconnect suggests that critical molecular linkers connecting the ER
101 network to the mitochondrial transport machinery are missing from our current understanding.

102 *C19orf12*, a gene mutated in a severe autosomal recessive form of HSP (SPG43) as well as a form of
103 neurodegeneration with brain iron accumulation (NBIA), represents a candidate for this missing link^{39–42}.
104 Previous studies have reported that *C19orf12* localizes to both the ER and mitochondria under overexpression
105 conditions and implicated the protein in broad cellular process like autophagy and lipid metabolism^{43,44}.
106 However, the precise subcellular localization of the endogenous protein remains controversial, and its primary
107 physiological function—specifically the molecular mechanism linking its dysfunction to axonal
108 degeneration—remains elusive. Here, we identify *C19orf12* as an ER-anchored organizer of mitochondrial
109 transport complex that enriches at ER-mitochondria contact sites. Based on these distinct characteristics, we
110 propose to rename this protein **EMTRAS** (**E**ndoplasmic reticulum–**a**nchored **M**itochondrial **T**rafficking
111 **S**caffold). We demonstrate that EMTRAS is indispensable for maintaining axonal integrity, as its deficiency
112 drives progressive motor impairment in mice and distal mitochondrial depletion in neurons. Mechanistically,
113 we show that EMTRAS functions as a Ca²⁺-tunable scaffold that bridges the ER to the mitochondrial surface,
114 promoting the assembly of the Miro1–Kinesin-1 complex. Our findings reveal that ER-mitochondria contacts
115 serve as critical logistical hubs for organelle transport, providing a unifying mechanism for the pathogenesis
116 of HSP.

117

118

119 **Results**

120 **EMTRAS deficiency leads to progressive motor impairment and HSP-like pathology in mice**

121 To determine the physiological function of the NBIA- and HSP-associated protein EMTRAS (encoded by
122 *C19orf12*), we first characterized the expression profile of EMTRAS in the mouse brain. Immunoblotting and
123 RT-qPCR analysis of wild-type mouse (*Emtras*^{+/+}) lysates revealed that EMTRAS expression progressively
124 increases during postnatal development (from P5 to P60), coinciding with the period of neuronal maturation
125 **(Extended Data Fig. 1a, b)**.

126 We next generated constitutive knockout mice (*Emtras*^{-/-}) using a CRISPR-Cas9 targeting strategy
127 **(Extended Data Fig. 1c)**, and confirmed the complete loss of *Emtras* transcripts by RT-qPCR **(Extended Data**
128 **Fig. 1d)**. Clinically, *C19orf12* mutations cause both NBIA and Spastic Paraplegia type 43 (SPG43),
129 characterized by progressive spasticity and motor dysfunction⁴⁰. Our mouse model robustly recapitulated these
130 features. Notably, aged *Emtras*^{-/-} mice (15 months) developed pronounced hindlimb clasp reflexes and
131 abnormal gait patterns indicative of pyramidal tract dysfunction **(Fig. 1a-d)**. Comprehensive behavioral testing
132 revealed significant deficits in motor coordination and neuromuscular strength: *Emtras*^{-/-} mice showed reduced
133 latency on the rotarod, increased time to descend the pole, difficulty in the beam-walking test, and weakened
134 grip strength compared to age-matched controls **(Fig. 1e-h)**. Although active motor challenges were terminated,
135 we continued to monitor spontaneous behaviors and general health longitudinally. Automated gait analysis in
136 aged mice revealed a higher stride Symmetry Index (SI stride) and increased Coefficient of Variation (CV
137 base), quantitatively confirming persistent gait instability **(Fig. 1i-k)**.

138 Furthermore, longitudinal monitoring revealed a late-onset systemic phenotype, characterized by
139 progressive weight loss and increased mortality in *Emtras*^{-/-} geriatric mice **(Fig. 1l-n)**. These data establish
140 *Emtras*^{-/-} mice as a valid model for HSP and indicate that EMTRAS is essential for maintaining long-term
141 motor function.

142 **EMTRAS is essential for axonal mitochondrial transport and bioenergetics in hippocampal neurons**

143 We next investigated the cellular basis of these motor deficits. HSP is characterized by the specific
144 degeneration of long corticospinal axons, a “dying-back” pathology strongly implicating defects in long-range
145 axonal transport^{37,38}, and NBIA is characterized by brain iron accumulation and prominent axonal spheroids,
146 consistent with impairment in axonal transport^{41,42}. Given the crucial role of mitochondria in sustaining
147 synaptic energy homeostasis⁴, we hypothesized a defect in axonal mitochondrial transport. In primary
148 hippocampal neurons isolated from *Emtras*^{-/-} mice, time-lapse imaging revealed a severe impairment in
149 mitochondrial motility **(Fig. 2a)**. While *Emtras*^{+/+} neurons displayed robust bidirectional movement, *Emtras*^{-/-}
150 neurons exhibited a marked reduction in the fraction of motile mitochondria and a corresponding increase in
151 stationary states **(Fig. 2a, b)**. This phenotype was further validated in *Emtras* knockdown (sh*Emtras*) neurons
152 using acute shRNA, which recapitulated the transport defects **(Fig. 2c, d)**. A direct consequence of failed
153 anterograde transport is the inability to replenish mitochondria at distal sites. Indeed, imaging of axonal
154 terminals revealed a progressive depletion of mitochondria towards the distal end in *Emtras*^{-/-} neurons

155 compared to controls (**Fig. 2e**). Quantification of mitochondrial fluorescence intensity specifically within
156 axonal tips confirmed a significant reduction in mitochondrial payload (**Fig. 2f-h**).

157 Mitochondria are essential for local ATP synthesis to fuel synaptic transmission. We therefore asked whether
158 this spatial depletion compromised neuronal bioenergetics. Using the ratiometric ATP probe ATeam1.03⁴⁵
159 (single-excitation, dual-emission readout), we detected lower ATP levels (F_{YFP}/F_{CFP} ratio) at distal axons in
160 both *Emtras*^{-/-} and *shEmtras* neurons to controls (**Fig. 2i-l**). Collectively, these data demonstrate that EMTRAS
161 is indispensable for sustaining the population of motile mitochondria required to supply the distal axon and
162 maintain neuronal energy homeostasis.

163

164 **EMTRAS deficiency induces perinuclear mitochondrial clustering**

165 To dissect the molecular mechanism underlying this transport defect, we utilized U2OS cells as a tractable
166 model, since EMTRAS is broadly expressed across tissues⁴⁶ (**Extended Data Fig. 2a**). Consistent with the
167 neuronal phenotype, loss of EMTRAS resulted in a striking redistribution of the mitochondrial network:
168 mitochondria retracted from the cell periphery and accumulated heavily in the perinuclear region (**Fig. 3a, b**).
169 Quantitative analysis using asymmetry coefficient confirmed a significant reduction in mitochondrial
170 spreading (**Fig. 3c**), and the proportion of cells exhibiting severe clustering increasing from ~25% in wild-type
171 (WT) to ~80% in U2OS knockout (KO) cells (**Fig. 3d**). Crucially, this transport defect was specific to
172 mitochondria. The distribution and protein levels of lysosomes (LAMP1) remained unaffected (**Fig. 3a, c, d**;
173 **Extended Data Fig. 2b**), ruling out a generalized impairment of organelle trafficking. Moreover,
174 mitochondrial membrane potential ($\Delta\psi_m$) was fully preserved in KO cells (**Extended Data Fig. 2c, d**),
175 indicating that the clustering is not a secondary consequence of mitochondrial dysfunction. Finally, we
176 confirmed that this phenotype is a conserved mechanism, as identical mitochondrial clustering was observed
177 across multiple cell lines, including COS7 and A549 cells (**Extended Data Fig. 3**).

178 To link this phenotype to HSP pathology, we performed rescue experiments with human *EMTRAS*
179 variants^{39,41}. Re-expression of full-length EMTRAS in KO cells fully restored the peripheral mitochondrial
180 network whereas HSP pathogenic mutants G58R and A63P, which were diffuse in the cytosol, failed to rescue
181 the phenotype (**Fig. 3e-g**; **Extended Data Fig. 2e**). Notably, the A34V mutant retained ER localization similar
182 to WT but still failed to reinstate normal distribution (**Fig. 3e**). This result implies that while membrane
183 targeting is necessary, it is insufficient for function; the A34V mutation likely disrupts a specific effector
184 interaction required for mitochondrial positioning.

185 Crucially, to determine whether these transport defects in mice and cells were secondary to the degradation
186 of transport machinery, we analyzed protein abundance. Immunoblotting of whole brain and spinal cord lysates
187 from *Emtras*^{-/-} mice, as well as lysates from *EMTRAS* KO cells, revealed that total levels of key transport
188 components (like Miro1, Kif5b, KLCs) and mitochondrial markers (Tom20) remained unchanged (**Extended**
189 **Data Fig. 4**). This indicates that the observed phenotypes arise from the functional impairment of the transport
190 machinery rather than the loss of its components.

191 **EMTRAS is a dynamic ER-anchored protein enriched at ER–mitochondria contact sites**

192 Having established that EMTRAS deficiency causes mitochondrial clustering, we next sought to define its
193 precise subcellular localization and dynamics to understand how EMTRAS exerts this spatial control.
194 Consistent with previous reports⁴⁰, overexpressed EMTRAS showed both ER and mitochondrial localization
195 (**Extended Data Fig. 5a**). To test this at the endogenous level without overexpression artifacts, we established
196 EMTRAS-Halo-3×Flag and EMTRAS-ALFA knock-in U2OS cells using CRISPR-Cas9 (**Fig. 4a, b**;
197 **Extended Data Fig. 5b**). At endogenous levels, all EMTRAS signals co-localize with the ER marker Sec61β,
198 with slight enrichment at ER-mitochondrial contact sites (**Fig. 4a; Extended Data Fig. 5b**), suggesting that
199 EMTRAS is an ER-associated protein that may specifically function at the interface between these two
200 organelles.

201 However, standard subcellular fractionation⁴⁷ yielded a paradoxical result: while the protein appeared ER-
202 associated in imaging, biochemical analysis of U2OS and HEK293T lysates showed that the vast majority of
203 EMTRAS was in the cytosolic fraction, with minimal signal in the crude mitochondrial (Mc) or ER-enriched
204 fractions (**Extended Data Fig. 5c, d**). This discrepancy suggested that EMTRAS might be loosely or
205 dynamically associated with the ER membrane, making it susceptible to dissociation during cell lysis. To test
206 this hypothesis, we performed fractionation following crosslinking to stabilize transient interactions. Strikingly,
207 under crosslinking conditions, the endogenous EMTRAS pool shifted from the cytosolic fraction to the ER-
208 bound fractions (**Fig. 4c**). Single-molecule tracking (SMT) further confirmed that EMTRAS molecules diffuse
209 along ER tubules but exhibit transient confinement specifically at regions overlapping with mitochondria (**Fig.**
210 **4d**).

211 Collectively, these biochemical and biophysical data demonstrate that EMTRAS is not a stable integral
212 transmembrane protein, but rather a dynamic ER-anchored protein that transiently enriches at ER–
213 mitochondria contact sites.

214 **ER membrane anchoring is necessary for EMTRAS function**

215 To test whether ER anchoring is required for EMTRAS function, we performed rescue experiments with
216 chimeric constructs. A mutant lacking the previously predicted hydrophobic transmembrane-like region
217 (Δ pTM) failed to rescue mitochondrial clustering (**Fig. 4e-h**). Our earlier biochemical and imaging data (**Fig.**
218 **3b, c; Extended Data Fig. 5c, d**) established that EMTRAS is not an integral membrane protein, and this
219 predicted hydrophobic region does not function as a canonical transmembrane domain. However, the loss-of-
220 function phenotype of the Δ pTM mutant indicates that this hydrophobic region is critical for EMTRAS's
221 dynamic association with the ER membrane (**Fig. 4e**). Collectively, these results confirm that ER membrane
222 association is essential for EMTRAS's ability to regulate mitochondrial distribution.

223 To further confirm that ER anchoring is indispensable for EMTRAS's function, we next tested whether
224 replacing its native hydrophobic region with heterologous ER-targeting sequences could substitute for the
225 endogenous motif. We generated chimeric EMTRAS constructs by replacing the predicted hydrophobic region
226 with ER-targeting transmembrane domains from Atlantin-3 (ATL3-TM) or EI24 (EI24-TM), while also

227 generating a control construct targeting EMTRAS to the mitochondrial outer membrane using the MFN2
228 transmembrane domain (MFN2-TM). Remarkably, the ER-anchored chimeric constructs (ATL3-TM and EI24-
229 TM) fully rescued the mitochondrial distribution defects in *EMTRAS* KO cells. In contrast, the mitochondria-
230 targeted MFN2-TM chimeric construct failed to restore normal mitochondrial spreading (**Fig. 4e-h; Extended**
231 **Data Fig. 5e**). Thus, we conclude that EMTRAS function is strictly dependent on its specific localization to
232 the ER membrane.

233 **EMTRAS is required for Kinesin-1 recruitment and interacts with mitochondrial transport machinery**

234 The prominent perinuclear clustering of mitochondria observed in *EMTRAS*-KO cells suggests a specific
235 deficit in anterograde transport. We therefore hypothesized that EMTRAS loss might impair the recruitment
236 of the anterograde motor Kinesin-1 heavy chain (Kif5b). To test this, we visualized the endogenous association
237 between motor proteins and mitochondria using the Proximity Ligation Assay (PLA). Strikingly, the PLA
238 signals representing the interaction between Kif5b and the mitochondrial marker Tom20 were drastically
239 reduced in *EMTRAS*-KO cells and *Emtras*^{-/-} brain tissues (**Fig. 5a-d**). In contrast, the interaction between
240 Dynein and mitochondria remained unchanged in *EMTRAS*-KO cells (**Fig. 5a, b**). This indicates that EMTRAS
241 is specifically required for the attachment of the anterograde transport machinery.

242 To identify the molecular machinery engaged by EMTRAS, we performed affinity purification-mass
243 spectrometry (AP-MS) using purified EMTRAS as bait (**Extended Data Fig. 6a**). This unbiased screen
244 identified Kif5b and the mitochondrial Rho GTPase Miro1/2 as potential interactors of EMTRAS (**Extended**
245 **Data Fig. 6b**). Given the high sequence homology between the two Rho GTPases and the higher peptide
246 coverage observed for Miro1, we focused our mechanistic characterization on Miro1 as the representative
247 isoform.

248 To validate these interactions and confirm their specificity, we first performed co-immunoprecipitation (Co-
249 IP) assays. These demonstrated robust interactions between EMTRAS and both Miro1 and Kif5b (**Fig. 5e, f**).
250 Notably, the canonical mitochondrial adaptor TRAK1 was absent from the EMTRAS interactome, and Co-IP
251 assays further confirmed that EMTRAS does not physically associate with TRAK1 (**Extended Data Fig. 6c**),
252 indicating that EMTRAS engages the transport machinery through a distinct, specific interface rather than
253 binding promiscuously to all transport adaptors. Importantly, although the HSP-associated A34V localized
254 correctly to the ER (**Fig. 3e**), it exhibited significantly reduced binding affinity for both Miro1 and Kif5b (**Fig.**
255 **5e, f**). This molecular defect—the inability to effectively recruit the motor complex—provides a mechanistic
256 explanation for why the A34V variant fails to support mitochondrial transport and causes disease.

257 To further confirm the EMTRAS-Miro1-Kif5b interactions at endogenous levels, we utilized U2OS cells
258 harboring a knock-in 3×Flag-Miro1 allele. Under DSP cross-linking conditions, endogenous EMTRAS co-
259 immunoprecipitated with Miro1 (**Fig. 5g**). This interaction was preserved under mild detergent conditions
260 while simultaneously recovering the known Miro1-Kif5b/TRAK1/TRAK2 assemblies (**Fig. 5h**), confirming
261 physiological complex formation.

262 Furthermore, *in vitro* pull-down assays using purified recombinant proteins confirmed that EMTRAS acts
263 as a direct physical linker, binding to both Miro1 and Kif5b (**Fig. 5i, j**). Detailed domain mapping using
264 truncation mutants revealed distinct binding modes for these partners: EMTRAS specifically recognizes the
265 C-terminal cargo-binding tail of Kif5b (amino acids 744–963)—the canonical site for adaptor attachment—
266 whereas binding to Miro1 required the presence of multiple domains, likely to preserve the structural stability
267 required for the interaction (**Extended Data Fig. 6d-j**).

268 Intriguingly, during these biochemical characterizations, we observed that purified EMTRAS protein
269 formed spherical droplets under molecular crowding conditions exhibiting fusion and fission dynamics,
270 characteristic of liquid-liquid phase separation (LLPS) (**Extended Data Fig. 7a, Extended Data Fig. 8a, b**).
271 In contrast, neither Miro1 nor Kif5b formed condensates on their own under identical conditions (**Extended**
272 **Data Fig. 7b, c**). However, EMTRAS was able to recruit both Miro1 and Kif5b into these condensates
273 (**Extended Data Fig. 7d, Extended Data Fig. 8c-g**), suggesting that the transport machinery might be
274 assembled within specialized phase-separated compartments at contact sites.

275 **EMTRAS scaffolds the assembly of the Miro1–Kinesin-1 anterograde transport complex**

276 Having established that EMTRAS directly binds the transport machinery, we investigated why its loss leads to
277 motor detachment. Mechanistically, we hypothesized that EMTRAS acts as a scaffold to stabilize the Miro1–
278 Kif5b complex. Consistent with this, the interaction between Miro1 and Kif5b was significantly reduced in
279 *EMTRAS*-KO cells compared to WT controls (**Fig. 5k, l**). Moreover, in the *in vitro* binding assays, the presence
280 of EMTRAS promoted the association between Kif5b and Miro1 (**Fig. 5m**). These data demonstrate that
281 EMTRAS is essential for the efficient assembly of the Miro1–Kinesin-1 complex.

282 To define the pathway specificity and hierarchy of EMTRAS, we examined its relationship with the
283 canonical transport adaptors Miro1 and TRAK1. Given that EMTRAS does not physically bind TRAK1
284 (**Extended Data Fig. 6c**), we asked if they function through independent mechanisms. Overexpression of
285 TRAK1 is known to drive mitochondrial hyper-spreading^{20,48}. We found that TRAK1 overexpression induced
286 mitochondrial extension not only in WT cells but also in *EMTRAS*-KO cells to a similar extent (**Extended**
287 **Data Fig. 9a-c**). This ability of TRAK1 to bypass EMTRAS deficiency indicates that EMTRAS functions
288 independently of the TRAK1-mediated transport pathway.

289 In contrast, we observed a distinct dependency relationship between EMTRAS and Miro1. While
290 overexpression of Miro1 induced a slight outward displacement of mitochondria and promoted hyper-fusion¹⁶,
291 it failed to effectively restore the global mitochondrial spreading in *EMTRAS*-KO cells (**Extended Data Fig.**
292 **9d-f**). This indicates that increasing Miro1 dosage alone is insufficient to drive long-range transport in the
293 absence of EMTRAS. To further clarify this dependency, we utilized Miro1/2 double-knockout cells, which
294 exhibited severe mitochondrial clustering^{20,49}. Reintroducing EMTRAS into these cells failed to rescue the
295 clustering phenotype, confirming that EMTRAS cannot function independently of Miro1/2 (**Extended Data**
296 **Fig. 9g-i**). Together, these results establish a mutually dependent relationship, with EMTRAS being essential

297 for Miro1 to mediate efficient mitochondrial transport, and Miro1/2 serving as the obligate mitochondrial
298 partners for EMTRAS to scaffold the transport complex.

299 **Ca²⁺ regulates EMTRAS-mediated transport assembly and mitochondrial motility**

300 Miro1 contains calcium-sensing EF-hand motifs, and previous studies have suggested that binding of cytosolic
301 Ca²⁺ to Miro1 can trigger mitochondrial arrest^{21,22}. Building on this regulatory role of Ca²⁺ in Miro1-mediated
302 mitochondrial dynamics, we hypothesized that the EMTRAS-dependent assembly of the transport complex
303 might also be sensitive to calcium fluctuations—an idea further supported by our RNA-seq analysis of
304 *EMTRAS* deficient cells. Specifically, RNA-seq revealed that “calcium ion binding” was among the top
305 upregulated functional categories in *EMTRAS*-KO cells (**Extended Data Fig. 10**), a transcriptional signature
306 hinting at a compensatory response to altered calcium handling.

307 We performed *in vitro* GST pull-down assays in the presence of varying free Ca²⁺ concentrations ranging
308 from 0 (EGTA) to 1 mM (**Fig. 6a**). Quantification revealed a “bell-shaped” binding dependence: the affinity
309 between EMTRAS and Miro1 increased from basal levels to a maximum at ~1 μM Ca²⁺ and declined at higher
310 concentrations (**Fig. 6a, b**). Notably, previous studies have estimated that local Ca²⁺ concentrations at ER–
311 mitochondria contact sites fluctuate within the micromolar range (typically 1–20 μM) during signaling events.
312 This suggests that physiological Ca²⁺ levels promote complex formation, whereas supraphysiological levels
313 are inhibitory.

314 Consistent with this binding affinity data, we found that the phase separation of the complex is also
315 exquisitely tuned by calcium. Crucially, the phase separation of EMTRAS protein alone was unaffected by
316 Ca²⁺ fluctuations, maintaining stable droplets across all tested concentrations (**Extended Data Fig. 11a-c**). The
317 formation of EMTRAS–Miro1 co-condensates was significantly enhanced at physiological Ca²⁺
318 concentrations (~1–10 μM) but was suppressed under calcium-free or calcium-overload conditions (**Extended**
319 **Data Fig. 11d-i**). This indicates that Ca²⁺ acts as a specific switch to regulate the recruitment of the transport
320 machinery rather than the structural integrity of the EMTRAS scaffold itself.

321 To confirm that this regulation relies on the calcium-sensing ability of Miro1, we generated a Miro1 mutant
322 with disrupted EF-hand domains (Miro1-ΔEF). Strikingly, the interaction between EMTRAS and Miro1-ΔEF
323 became insensitive to calcium fluctuations, maintaining a constant binding affinity across all tested
324 concentrations (**Fig. 6c, d**). This explicitly demonstrates that Miro1 acts as the calcium sensor that tunes the
325 assembly of the transport machinery.

326 To validate the physiological relevance of this regulation in living cells, we examined the relationship
327 between local calcium dynamics and mitochondrial motility using the mitochondrial surface-localized calcium
328 sensor GCaMP6f-Tom5 (**Fig. 6e**). Live-cell time-lapse imaging revealed that mitochondria exhibit
329 spontaneous, transient calcium “flashes” on their surface. By tracking individual mitochondria, we observed a
330 striking biphasic relationship rather than a simple negative correlation.

331 Consistent with established models where calcium influx or matrix calcium accumulation triggers
332 mitochondrial arrest²⁴, mitochondrial speed progressively declined as surface calcium increased to high levels
333 (**Fig 6f, Fig 6g Bin 3–5**). However, we unexpectedly observed that motility was reduced at low calcium levels
334 (**Fig 6g Bin 1**) and significantly increased to a peak at intermediate calcium ranges (**Fig 6g Bin 2**). This
335 biphasic profile indicates that physiological surface Ca²⁺ is not merely a "brake" but acts as a critical rheostat:
336 basal-to-moderate Ca²⁺ levels are required to prime the mitochondrial trafficking assembly for optimal motility,
337 while calcium overload triggers arrest. We therefore propose that surface Ca²⁺ tunes the probability of
338 EMTRAS–Miro1 assembly, providing a key modulatory layer within mitochondrial trafficking control.

339 Discussion

340 Our study uncovers the molecular mechanism of *C19orf12*, a gene linked to neurodegeneration and
341 impairments in axonal transport^{40,41}, identifying its protein product as an ER-anchored regulator that confers
342 precise ER-mediated control over mitochondrial transport (**Fig. 7**). Based on its essential role in orchestrating
343 these organelle dynamics, we refer to this protein as EMTRAS. By delineating the function of EMTRAS, we
344 establish mitochondrial transport regulation as a novel functional dimension of ER–mitochondria contact sites,
345 expanding their role beyond the canonical functions of lipid transfer and calcium signaling³⁰. By combining
346 mouse genetics, neuronal physiology, and biochemical reconstitution, we demonstrate that loss of EMTRAS
347 leads to a “dying-back” depletion of axonal mitochondria, energetic failure at synapses, and the progressive
348 spastic paraplegia phenotype common to patients with HSP and NBIA.

349 Our *Emtras* knockout mice robustly shared the clinical features of SPG43 and NBIA, including progressive
350 spasticity, muscle weakness, and gait instability⁴⁰. These phenotypes was also observed in a recently reported
351 *Emtras*-deficient model⁵⁰, confirming that EMTRAS is indispensable for the long-term maintenance of the
352 corticospinal tract. At the cellular level, we pinpoint the primary defect to a failure in anterograde
353 mitochondrial transport. This transport deficit creates a “supply chain crisis” in long axons: while the soma
354 retains a clustered mitochondrial mass, distal terminals become devoid of organelles and depleted of ATP. This
355 spatial bioenergetic mismatch offers a parsimonious explanation for the length-dependent degeneration of
356 axons in HSP and axonal spheroids in NBIA, linking the molecular defect in EMTRAS directly to the
357 vulnerability of distal synapses^{8,37}.

358 A central finding of our work is the definition of EMTRAS’s molecular identity as a dynamic ER-anchored
359 scaffold. Previous studies relying on overexpression often observed EMTRAS on both ER and mitochondria,
360 leading to ambiguity about its primary site of action⁴⁰. By leveraging endogenous tagging and single-molecule
361 tracking, we show that physiological EMTRAS resides on the ER membrane, concentrating transiently at
362 contact sites. Crucially, our chimeric rescue experiments provide compelling evidence that ER anchoring is
363 the critical spatial determinant for EMTRAS function. Targeting EMTRAS to the mitochondrial outer
364 membrane failed to rescue the transport defect, proving that EMTRAS must operate from the ER side of the
365 interface. This finding conceptually advances our understanding of organelle transport by proposing that the
366 motive force for mitochondria is not solely intrinsic to the organelle but is orchestrated by the ER network^{30,32}.
367 We propose that EMTRAS acts as a molecular staple, stabilizing the interaction between the mitochondrial

368 receptor Miro1 and the cytosolic motor Kinesin-1 specifically at sites where the ER lattice contacts the
369 mitochondrion. Furthermore, our data suggest that this scaffolding function is potentiated by liquid–liquid
370 phase separation (LLPS). This biophysical mechanism allows the ER to rapidly concentrate dilute cytosolic
371 motors (Kinesin-1) at specific contact sites, creating a high-density “reaction crucible” for transport assembly.
372 This phase-separated compartment offers a compelling explanation for how the transport machinery achieves
373 the high local stoichiometry required for effective motility within the crowded cytoskeletal environment.

374 Our biochemical mapping reveals that EMTRAS exhibits exquisite specificity, binding the Kinesin-1/Miro1
375 axis while excluding the adaptor TRAK1. This distinction is functionally relevant: while TRAK1
376 overexpression can bypass EMTRAS loss (likely by driving hyper-motility through an independent pathway),
377 Miro1 overexpression cannot. This places EMTRAS as a specific, obligatory co-factor for Miro1-dependent
378 transport rather than a redundant component. The disease-causing mutation A34V further underscores this
379 specificity; despite localizing correctly to the ER, A34V fails to bind the Miro1–Kinesin-1 complex. This
380 suggests that the pathogenesis of SPG43 and some forms of NBIA arise not from protein misfolding or
381 aggregation, but from a precise loss of effector engagement, resulting in “empty” ER-mitochondria contacts
382 that fail to load motors.

383 Finally, our data unveil a novel regulatory layer where local Ca^{2+} dynamics tune the assembly of the transport
384 machinery. Crucially, we found that both the molecular binding affinity and the phase separation of the
385 complex are exquisitely tuned by calcium. We identified a “bell-shaped” dependency where the EMTRAS–
386 Miro1 interaction and its co-condensation is optimal at physiological microdomain concentrations ($\sim 1\text{--}10\ \mu\text{M}$)
387 characteristic of contact sites^{26,27} but is suppressed under calcium-free or calcium-overload conditions. This
388 relies on the calcium-sensing EF-hands of Miro1, as an EF-hand mutant became insensitive to this regulation.
389 Physiologically, this mechanism allows the transport machinery to distinguish between the “basal” state (low
390 affinity), the “active signaling” state (high affinity at contacts), and the “overload” state
391 (disassembly/arrest)^{21,22}. In the context of HSP, this sensitivity suggests that EMTRAS-mediated transport is
392 uniquely positioned to respond to neuronal activity patterns, and its failure may render axons unable to adapt
393 mitochondrial distribution to metabolic demand.

394 In summary, we define EMTRAS as an essential ER-based regulator that couples the mitochondrial transport
395 machinery to the ER network. Our findings not only clarify the pathogenic mechanism of SPG43 but also
396 highlight the ER–mitochondria interface as a critical command center for the logistic support of long axons.

397

398 **Author Contributions**

399 X.P. designed and conducted most of the experiments and wrote the manuscript. S.Z. conducted some
400 molecular biology experiments, cell biology experiments, and data analysis. P.L. performed single-molecule
401 imaging experiments. Y.W. helped with some data analysis. Y.C., X.F., X.H., Y. W., N.H., B.L. helped with the
402 experimental design. P.Z., C.B., J.C. and J.T. are the senior authors who conceived and designed the project.
403 All authors approved the final version of the manuscript.

404

405 **Competing interests**

406 The authors declare no competing interests.

407

408 **Acknowledgements**

409 The authors thank the National Center for Protein Sciences at Peking University in Beijing, China, for
410 assistance with confocal microscopy imaging (by Chunyan Shan, Liqin Fu, Wenling Gao, and Siying Qin),
411 flow cytometry (by Liying Du), mass spectrometry (by Dong Liu and Qi Zhang), and schematic illustrations
412 (by Jun Hu). We thank Pathology core, school of College of Future Technology at Peking University in Beijing,
413 China, for assistance with paraffin sample embedding, sectioning and HE staining (by Xueting Sun and
414 Xuelian Wang). This work was supported by the National Natural Science Foundation of China (32370732,
415 32570806). The study was also supported in part by the Center for Life Sciences, School of Life Sciences of
416 Peking University, the MOE Key Laboratory of Cell Proliferation and Differentiation of China, the State Key
417 Laboratory of Membrane Biology of China, and the Massachusetts General Hospital..

418

419 **EXPERIMENTAL MODEL AND SUBJECT DETAILS**

420 **Animals**

421 C57BL/6J mice (6–8 weeks old) were obtained from Beijing Vital River Laboratory Animal Technology.
422 *EMTRAS* (encoded by *C19orf12*) knockout mice were generated by Cyagen Biosciences using CRISPR–
423 Cas9 technology. sgRNAs targeting the murine *EMTRAS* gene were designed as follows: forward 5′-
424 AAATGATTATGAGTCCAGAC-3′ and reverse 5′-TGGCGGCTTACAATCAATGC-3′. F0 heterozygous
425 mice were backcrossed to wild-type C57BL/6J mice for two generations, and F3 heterozygotes were
426 intercrossed to generate homozygous *Emtras*^{-/-} knockout mice. All mice were housed in specific pathogen-free
427 (SPF) facilities at the Experimental Animal Center of Peking University. All animal procedures were conducted
428 in strict accordance with protocols approved by the Institutional Animal Care and Use Committee (IACUC) of
429 Peking University.

430

431 **Cell culture**

432 U2OS, HeLa, HEK-293T, and COS7 cells were cultured in Dulbecco's Modified Eagle's Medium (DMEM,
433 CellMax, CGM101.06) supplemented with 10% (v/v) fetal bovine serum (FBS) and penicillin (100
434 units/mL)/streptomycin (100 µg/mL). A549 cells were cultured in Ham's F-12K (Kaighn's) medium
435 (Meiluncell, PWL011) supplemented with FBS and antibiotics. Primary hippocampal neurons isolated from
436 embryonic day 16.5 (E16.5) mouse brains were cultured in Neurobasal-A medium (Gibco, 10888022)
437 supplemented with 2% (v/v) B-27 (Gibco, 17504-044) and 1% (v/v) GlutaMAX (Gibco, 35050-061). All cells
438 were maintained at 37°C in a humidified incubator with 5% CO₂.

439

440 **METHOD DETAILS**

441 **plasmids and molecular cloning**

442 All plasmids were generated using 2X MultiF Seamless Assembly Mix (ABclonal). All DNA fragments were
443 amplified by PCR from cDNA or genomic DNA templates. All plasmid sequences were verified using sanger
444 sequencing (RuiBiotech).

445

446 **Transfection and lentiviral transduction**

447 For HEK293T cells, transfections were performed using Polyethylenimine (PEI; Polysciences, 23966-1) at 60%
448 confluency. Medium was replaced 6 h post-transfection, and cells were harvested after 24 h. For other cell

449 lines, transfections were carried out using Omni transfection reagent (EZ Biosystems, EZT-OMNI). For
450 lentivirus production, HEK293T cells were co-transfected with the transfer plasmid, psPAX2, and pMD2.G.
451 After 6 hours, the medium was replaced with DMEM containing 20% FBS. Viral supernatants were collected
452 48–72 h post-transfection, filtered, and used to infect target cells. Primary neurons were infected at DIV 3 and
453 analyzed at DIV 8.

454

455 **Generation of knockout and knock-in cell line**

456 Gene-edited cell lines were generated using CRISPR–Cas9. The following sgRNA sequences were used for
457 knockout cell lines:

458 human *EMTRAS* (*C19orf12*) (5'-TGGGGAGAGGAAGATGAAGG-3');

459 human *Miro1* (5'-TCTGGTGGAAATATAGTAGTA-3');

460 human *Miro2* (5'-ACAAGGTACCCGTGGTGC GC-3');

461 human *TRAK1* (5'-GAATGTTGTACTTCGATCCG-3').

462 For knock-in lines, donor templates were designed to tag endogenous *EMTRAS* (C-terminal 3×Flag-Halo-
463 ALFA, 5'-TGGGGAGAGGAAGATGAAGG-3') or *Miro1* (N-terminal 3×Flag-mScarlet, 5'-
464 TTCTTCATGTCGGCGGCTCT-3'). A549 *EMTRAS* knockdown cells were generated using siRNA (5'-
465 GCAACAGAGGCTCTTTAACGA-3') targeting the *EMTRAS* transcript.

466

467 **Western blotting**

468 Cells were lysed in loading buffer (50 mM Tris, pH 6.8, 1 mM DTT, 10% glycerol, 2% SDS, 0.1%
469 Bromophenol blue), and boiled at 100°C for 10 min. Samples were run on SDS-PAGE gels (GenScript) and
470 transferred to PVDF membranes. Membranes were blocked with 4% milk in TBST (20 mM Tris, pH 7.4, 150
471 mM NaCl, 0.1% Tween-20), and incubated with primary antibody at 4 °C overnight. After washing with TBST,
472 membranes were incubated with secondary antibody at room temperature for 2 h, followed by washing with
473 TBST. Signals were detected using SuperSignal Peroxidase Solution (Biosciences, TE0015-2) and captured
474 on X-ray film (FUJIFILM). Band intensities were quantified using Fiji software.

475

476 **Immunoprecipitation**

477 Cells were lysed in lysis buffer (50 mM Tris-HCl, 150 mM NaCl, 1 mM EDTA, 0.5% Triton X-100, pH 7.5)

478 containing protease inhibitor PMSF and cocktail on ice for 30 min. The cell lysates were centrifuged at 12,500
479 rpm for 10 minutes and supernatants were collected for input and immunoprecipitation by mixing with
480 antibody-conjugated Protein A/G beads for 2 h at 4°C. Beads were washed five times with lysis buffer, and
481 bound proteins were eluted in sample buffer at 100°C for 10 min for immunoblotting.

482

483 **Mass spectrometry analysis of EMTRAS**

484 For mass spectrometry, HEK293T cells expressing Strep-tagged EMTRAS or mouse brains (n=10) were lysed
485 in appropriate buffers (Cell lysis: 50 mM Tris-HCl pH 7.5, 750 mM NaCl, 1% Triton X-100, 0.1 mM Biotin;
486 Brain lysis: 50 mM Tris-HCl pH 7.5, 150 mM NaCl, 0.1% SDS, 0.5% sodium deoxycholate, 1% Triton X-
487 100). Lysates were centrifuged at 15,000 rpm at 4°C for 15 minutes and the supernatants were collected
488 separately. The cell lysate supernatant was then incubated with Strep-Tactin beads for 2 h at 4°C, followed by
489 three times beads washing with Wash Buffer 1 (50 mM Tris, 750 mM NaCl, 1% Triton X-100, pH 7.5). Mouse
490 brain lysate supernatants were subsequently incubated with beads for 2 h at 4°C. Following incubation, beads
491 were washed three times with Wash Buffer 1 and twice with Wash Buffer 2 (50 mM Tris, 150 mM NaCl, pH
492 7.5) to remove high-salt contaminants. With supernatant discarded, loading buffer was added to the beads.
493 Eluted proteins were separated by SDS-PAGE, stained with Coomassie Blue, and excised for LC-MS/MS
494 analysis.

495

496 **Subcellular fractionation**

497 The isolation of subcellular fractions was conducted as previously described⁴⁷. Briefly, after collection and
498 homogenization, cells were centrifuged for 5 min at 600g twice to remove unbroken cells and nuclei.
499 Supernatant was collected and centrifuged for 10 min at 7,000g twice and the pellet was crude mitochondria
500 while the supernatant was plasma membrane, lysosomes, microsomes and cytosol. The cytosol supernatant
501 was centrifuged for 30 min at 20,000g and the supernatant was collected and further centrifuged for 1 h at
502 100,000g. The pellet was ER while the supernatant was cytosol. To obtain pure mitochondria, crude
503 mitochondria pellet was suspended and centrifuged for 10 min at 10,000g to remove contaminations.

504 The crude mitochondrial fractions were resuspended in mitochondrial resuspension buffer and layered on
505 top a Percoll medium. Following centrifugation at 95,000g for 30 min, the crude MAMs fraction appeared as
506 a diffuse white band above, while a dense band containing purified mitochondria settled near the bottom of the
507 tube. Both MAM and pure mitochondria fractions were further centrifuged to eliminate the Percoll. All
508 fractions obtained were rapidly frozen using liquid nitrogen and stored at -80 °C until they were ready to be
509 used.

510

511 **RNA extraction and RNA-seq analysis**

512 For cells, RNA extraction was conducted by using the RNA Easy Fast Tissue/Cell Kit (TIANGEN; DP451).
513 mRNA library constructing and sequencing were performed by GENEWIZ from Azenta Life Sciences.
514 Libraries with different indexes were multiplexed and loaded on an Illumina Novaseq instrument for
515 sequencing using a 2×150 paired-end configuration according to the manufacturer's instructions. Raw
516 sequencing reads in FASTQ format were processed using Fastp (v0.24.1) to remove technical sequences and
517 low-quality bases. Clean reads were aligned to the Homo sapiens (GRCh38.107) using HISAT2 (v2.2.1)⁵¹.
518 Gene-level counts were quantified using HTSeq (v0.6.1). Reads overlapping exons were counted, and multi-
519 mapping reads or reads overlapping multiple genes were excluded. Differentially expressed genes (DEGs)
520 were identified using DESeq2 (v1.34.0) and genes with $|\log_2FC| \geq 1$ and $FDR < 0.05$ were classified as
521 differentially expressed.

522

523 **Prokaryotic expression, purification and *in vitro* binding assays**

524 GST-Kif5b, GST-Miro1, EMTRAS-6×His and MBP-Miro1 proteins were expressed in E. coli BL21 (DE3)
525 induced with 1 mM IPTG at 16°C for 12–16 h. Cells were lysed using sonication in GST lysis buffer (50mM
526 Tris-HCl, 250mM NaCl, 0.5% Triton X-100, pH=8.0), His buffer (50mM Tris-HCl, 300mM NaCl, 0.5% Triton
527 X-100, 2mM β-Mercaptoethanol and 20mM imidazole, pH=8.0), and MBP lysis buffer (20 mM Tris-HCl, 200
528 mM NaCl, 1 mM EDTA, 1 mM DTT (optional), pH 7.5) followed by centrifugation at 13,500 rpm for 15 min
529 at 4°C. The supernatant was collected and incubated with the respective affinity beads (GST-Sepharose, Ni-
530 NTA, or Amylose resin) at 4°C with rotation for 2 hours. Beads were washed five times with wash buffer
531 (50mM Tris-HCl, 450mM NaCl, 0.5% Tween-20, pH=7.5), and the EMTRAS-6×His was eluted using His
532 elution buffer (50mM Tris-HCl, 300mM NaCl, 0.5% Triton X-100, 2mM β-Mercaptoethanol and 250mM
533 imidazole, pH=8.0); MBP-Miro1 protein was eluted using MBP elution buffer (20 mM Tris-HCl, 200 mM
534 NaCl, 1 mM EDTA, 1 mM DTT (optional), 10mM maltose, pH 7.5); GST-Kif5b and GST-Miro1 protein was
535 eluted using GST elution buffer (50mM Tris-HCl, 250mM NaCl, 50 mM GSH, pH=8.0).

536 For pull-down assays, purified bait proteins bound to beads were incubated with prey proteins for 2 h at 4°C.
537 After five washes, bound complexes were eluted and analyzed by immunoblotting or Coomassie staining.

538

539 **Phase separation and FRAP assays**

540 Purified proteins were concentrated and buffer-exchanged into storage buffer (25 mM Tris-HCl pH 8.0, 500

541 mM KCl, 10% glycerol) using Amicon® Ultra filters (Millipore). After concentration, the protein was
542 aliquoted and rapidly frozen in liquid nitrogen, followed by storage at -80°C . The protein concentration was
543 determined using the BCA Protein Assay kit (Mei5bio, MF071-01). For phase separation, proteins were diluted
544 in low-salt buffer (25 mM Tris-HCl pH 8.0, 150 mM KCl) with or without PEG8000 and CaCl_2 in 384-well
545 plates. Droplets were visualized after indicated time of incubation.

546 For fluorescence recovery after photobleaching (FRAP) analysis of in vitro assembled condensates, particles
547 were chosen for initial photobleaching by corresponding fluorescent-protein laser for 0.5 s with laser power
548 50, and the fluorescence recovery was imaged at 2 s intervals for a total of about 1 min using a Zeiss LSM980
549 microscope.

550

551 **Immunofluorescence and imaging**

552 Cells were fixed with 4% paraformaldehyde in PBS for 30 min at 37°C and permeabilized with 0.1% Triton
553 X-100 in PBS for 10 min. After blocked with 4% BSA for 30 min, cells were incubated with primary antibodies
554 at 37°C for 2 hours, and further incubated with secondary antibodies in the dark at 37°C for 1 hour, followed
555 by three PBS washes respectively. Coverslips were mounted using a glycerol: PBS (1:1) solution containing
556 DAPI and stored at 4°C . Imaging was performed using a Zeiss LSM980 microscope equipped with a $63\times/1.4$
557 oil objective lens in Airyscan mode. Images were acquired using ZEN software (Carl Zeiss) and processed
558 with ZEN software or Fiji.

559

560 **Proximity ligation assay**

561 PLA (Sigma-Aldrich, DUO92101) was performed according to the manufacturer's instructions. Samples were
562 observed under a Zeiss LSM980 confocal microscope using the Airyscan function. The total intensity of the
563 PLA signal per cell was quantified using Fiji software.

564

565 **JC-1 staining**

566 Cells cultured in chamber slides were stained with $10\ \mu\text{g}/\text{mL}$ JC-1 working solution in a 37°C , 5% CO_2
567 incubator for 15 min. After PBS wash, cells were cultured in complete medium for live cell imaging. Imaging
568 was performed using a Zeiss LSM980 microscope equipped with a $63\times/1.4$ oil objective lens in Confocal mode.
569 Images were acquired using ZEN software (Carl Zeiss) and processed with ZEN software or Fiji.

570

571 **Mouse Behavioral Tests**

572 All behavioral tests were performed on age-matched mice trained 24 h prior to testing.

573 Hindlimb clasping: Mice were held by their tails for 10 s and scored on a scale of 0-3 based on the degree
574 of splaying outward from the abdomen. 0: the hindlimbs are fully spread and moving; 1: a retraction toward
575 the abdomen in >50% of one hindlimb; 2: a retraction toward the abdomen in >50% of both hindlimbs; and 3:
576 both hindlimbs fully retracted to the abdomen.

577 Balance beam: Mice were trained to walk across a horizontal beam (100 cm in length, 12 mm in width, and
578 50 cm in height) to their home cages and were recorded beam-walking using a video camera. Each mouse was
579 tested three times separately.

580 Forelimb grip: Mouse was placed over the grid with its forepaws grasping the grid. Gently pull the mouse
581 backward by its tail to ensure it holds on to the upper part of the grid while maintaining a horizontal torso.
582 Record the maximum grip strength value displayed on the screen. Each mouse was tested three times separately.

583 Pole test: Mice were positioned at the top of a vertical pole (50 cm high and 1 cm in diameter) and assessed
584 for their ability to descend the pole (with the snout leading) by measuring the time from the initiation of the
585 head-down movement until all four paws reached the platform. Each mouse was tested three times separately.

586 Rotarod: Mice were placed on the rod of the equipment rotating at 4 rpm for habitation until accelerating
587 the rotarod from 4 to 40 rpm in 5 min. The time until falling off the beam was recorded. Each mouse had a 10
588 min interval between trials and was tested three times per day for two consecutive days.

589 Treadmill test: Mouse running ability was tested on treadmill machine (SANSBIO). The treadmill speed
590 was set at 5 m/min for the first 5 min, then increased to 15 m/min for another 5 min, and finally set to 21 m/min
591 for 20 min. The test was terminated if the mouse was shocked for more than 3 s. The total running time and
592 the number of shocks received by the mouse were recorded. Each mouse was tested once per day for three
593 consecutive days.

594

595 **Neuropathological analysis**

596 For the collection of the adult mouse brain tissues, mice were anesthetized using Isoflurane (RWD, R510-22-
597 10) and perfused with ice-cold PBS to flush the blood and blood cells from the brain, followed by perfusion
598 with 4% PFA solution for fixation. The fixed samples were sent to the pathology center for paraffin sectioning,
599 and the resulting paraffin sections were subjected to immunofluorescence staining. After dewaxing with xylene
600 for 10 min twice, the paraffin sections were rehydrated with different gradients of ethanol (100%-95%-80%-
601 50%-25%) for 5 min each step. They were then washed with water and boiled in 100 mM sodium citrate buffer

602 (pH 6.0) for 10 min twice for antigen retrieval, followed by a 20 min incubation at room temperature, washed
603 with water and PBS. The subsequent permeabilization and blocking steps were consistent with those used in
604 cell immunofluorescence staining.

605

606 **ATP Imaging using ATeam1.03**

607 Neurons were transfected with the FRET-based ATP biosensor ATeam1.03-nD/nA/pcDNA3 (Addgene plasmid
608 #51958; a gift from Takeharu Nagai⁴⁵). Cells were imaged using a Zeiss LSM980 microscope equipped with
609 a 405 nm laser for CFP excitation. Dual-emission images were acquired for CFP (460–500 nm) and FRET/YFP
610 (520–550 nm). Image analysis was performed using Fiji software. Background was subtracted from both
611 channels, and the pixel-by-pixel ratio of FRET/CFP was calculated to generate pseudocolor ratio images.

612

613 **Quantification and statistical analysis**

614 The analysis of asymmetry coefficient was conducted as previously described³³. Quantitative data are shown
615 in column-scattered plots (GraphPad Prism). Significance values are indicated on data plots.

616

617 **References**

- 618 1. Lang, B. F., Gray, M. W. & Burger, G. Mitochondrial genome evolution and the origin of eukaryotes.
619 *Annu. Rev. Genet.* **33**, 351–397 (1999).
- 620 2. Friedman, J. R. & Nunnari, J. Mitochondrial form and function. *Nature* **505**, 335–343 (2014).
- 621 3. Suomalainen, A. & Nunnari, J. Mitochondria at the crossroads of health and disease. *Cell* **187**, 2601–
622 2627 (2024).
- 623 4. Sheng, Z.-H. Mitochondrial trafficking and anchoring in neurons: New insight and implications. *J. Cell*
624 *Biol.* **204**, 1087–1098 (2014).
- 625 5. De Vos, K. J., Grierson, A. J., Ackerley, S. & Miller, C. C. J. Role of Axonal Transport in
626 Neurodegenerative Diseases. *Annu. Rev. Neurosci.* **31**, 151–173 (2008).
- 627 6. Wang, X. *et al.* PINK1 and Parkin Target Miro for Phosphorylation and Degradation to Arrest
628 Mitochondrial Motility. *Cell* **147**, 893–906 (2011).
- 629 7. Blackstone, C. Cellular Pathways of Hereditary Spastic Paraplegia. *Annu. Rev. Neurosci.* **35**, 25–47
630 (2012).
- 631 8. Sheng, Z.-H. & Cai, Q. Mitochondrial transport in neurons: impact on synaptic homeostasis and
632 neurodegeneration. *Nat. Rev. Neurosci.* **13**, 77–93 (2012).
- 633 9. Hirokawa, N., Noda, Y., Tanaka, Y. & Niwa, S. Kinesin superfamily motor proteins and intracellular
634 transport. *Nat. Rev. Mol. Cell Biol.* **10**, 682–696 (2009).
- 635 10. Reck-Peterson, S. L., Redwine, W. B., Vale, R. D. & Carter, A. P. The cytoplasmic dynein transport
636 machinery and its many cargoes. *Nat. Rev. Mol. Cell Biol.* **19**, 382–398 (2018).
- 637 11. Hancock, W. O. Bidirectional cargo transport: moving beyond tug of war. *Nat. Rev. Mol. Cell Biol.* **15**,
638 615–628 (2014).
- 639 12. Trivedi, D. V., Nag, S., Spudich, A., Ruppel, K. M. & Spudich, J. A. The Myosin family of
640 mechanoenzymes: from mechanisms to therapeutic approaches. *Annu. Rev. Biochem.* **89**, 667–693
641 (2020).
- 642 13. Bocanegra, J. L. *et al.* The MyMOMA domain of MYO19 encodes for distinct Miro-dependent and
643 Miro-independent mechanisms of interaction with mitochondrial membranes. *Cytoskeleton* **77**, 149–166
644 (2020).
- 645 14. Zhao, Y. *et al.* Metaxins are core components of mitochondrial transport adaptor complexes. *Nat.*
646 *Commun.* **12**, 83 (2021).
- 647 15. Guo, X. *et al.* The GTPase dMiro is required for axonal transport of mitochondria to drosophila
648 synapses. *Neuron* **47**, 379–393 (2005).
- 649 16. Fransson, Å., Ruusala, A. & Aspenström, P. The atypical Rho GTPases Miro-1 and Miro-2 have
650 essential roles in mitochondrial trafficking. *Biochem. Biophys. Res. Commun.* **344**, 500–510 (2006).
- 651 17. Stowers, R. S., Megeath, L. J., Górska-Andrzejak, J., Meinertzhagen, I. A. & Schwarz, T. L. Axonal
652 transport of mitochondria to synapses depends on Milton, a novel drosophila protein. *Neuron* **36**, 1063–
653 1077 (2002).
- 654 18. Glater, E. E., Megeath, L. J., Stowers, R. S. & Schwarz, T. L. Axonal transport of mitochondria requires
655 milton to recruit kinesin heavy chain and is light chain independent. *J. Cell Biol.* **173**, 545–557 (2006).
- 656 19. Schwarz, T. L. Mitochondrial Trafficking in Neurons. *Cold Spring Harb. Perspect. Biol.* **5**, a011304–
657 a011304 (2013).
- 658 20. van Spronsen, M. *et al.* TRAK/Milton motor-adaptor proteins steer mitochondrial trafficking to axons
659 and dendrites. *Neuron* **77**, 485–502 (2013).
- 660 21. Wang, X. & Schwarz, T. L. The Mechanism of Ca²⁺-dependent regulation of Kinesin-mediated

- 661 mitochondrial motility. *Cell* **136**, 163–174 (2009).
- 662 22. MacAskill, A. F. *et al.* Miro1 Is a Calcium Sensor for Glutamate Receptor-Dependent Localization of
663 Mitochondria at Synapses. *Neuron* **61**, 541–555 (2009).
- 664 23. Niescier, R. F., Hong, K., Park, D. & Min, K.-T. MCU Interacts with Miro1 to Modulate Mitochondrial
665 Functions in Neurons. *J. Neurosci.* **38**, 4666–4677 (2018).
- 666 24. Chang, K. T., Niescier, R. F. & Min, K.-T. Mitochondrial matrix Ca²⁺ as an intrinsic signal regulating
667 mitochondrial motility in axons. *Proc. Natl. Acad. Sci.* **108**, 15456–15461 (2011).
- 668 25. Li, Y., Yang, Z., Zhang, S. & Li, J. Miro-mediated mitochondrial transport: A new dimension for
669 disease-related abnormal cell metabolism? *Biochem. Biophys. Res. Commun.* **705**, 149737 (2024).
- 670 26. Csordás, G. *et al.* Imaging Interorganelle Contacts and Local Calcium Dynamics at the ER-
671 Mitochondrial Interface. *Mol. Cell* **39**, 121–132 (2010).
- 672 27. Giacomello, M. *et al.* Ca²⁺ Hot Spots on the Mitochondrial Surface Are Generated by Ca²⁺ Mobilization
673 from Stores, but Not by Activation of Store-Operated Ca²⁺ Channels. *Mol. Cell* **38**, 280–290 (2010).
- 674 28. Wu, H., Carvalho, P. & Voeltz, G. K. Here, there, and everywhere: The importance of ER membrane
675 contact sites. *Science* **361**, eaan5835 (2018).
- 676 29. Cremer, T., Neefjes, J. & Berlin, I. The journey of Ca²⁺ through the cell – pulsing through the network
677 of ER membrane contact sites. *J. Cell Sci.* **133**, jcs249136 (2020).
- 678 30. Rowland, A. A. & Voeltz, G. K. Endoplasmic reticulum–mitochondria contacts: function of the junction.
679 *Nat. Rev. Mol. Cell Biol.* **13**, 607–615 (2012).
- 680 31. Abrisch, R. G., Gumbin, S. C., Wisniewski, B. T., Lackner, L. L. & Voeltz, G. K. Fission and fusion
681 machineries converge at ER contact sites to regulate mitochondrial morphology. *J. Cell Biol.* **219**,
682 e201911122 (2020).
- 683 32. Friedman, J. R. *et al.* ER tubules mark sites of mitochondrial division. *Science* **334**, 358–362 (2011).
- 684 33. Zheng, P. *et al.* ER proteins decipher the tubulin code to regulate organelle distribution. *Nature* **601**,
685 132–138 (2022).
- 686 34. Raiborg, C. *et al.* Repeated ER–endosome contacts promote endosome translocation and neurite
687 outgrowth. *Nature* **520**, 234–238 (2015).
- 688 35. Chen, S. *et al.* Dynamic interaction of REEP5–MFN1/2 enables mitochondrial hitchhiking on tubular
689 ER. *J. Cell Biol.* **223**, e202304031 (2024).
- 690 36. Kornmann, B., Osman, C. & Walter, P. The conserved GTPase Gem1 regulates endoplasmic reticulum–
691 mitochondria connections. *Proc. Natl. Acad. Sci.* **108**, 14151–14156 (2011).
- 692 37. Blackstone, C. Converging cellular themes for the hereditary spastic paraplegias. *Curr. Opin. Neurobiol.*
693 **51**, 139–146 (2018).
- 694 38. Denton, K. *et al.* Impaired mitochondrial dynamics underlie axonal defects in hereditary spastic
695 paraplegias. *Hum. Mol. Genet.* **27**, 2517–2530 (2018).
- 696 39. Meilleur, K. G. *et al.* Hereditary spastic paraplegia and amyotrophy associated with a novel locus on
697 chromosome 19. *neurogenetics* **11**, 313–318 (2010).
- 698 40. Landouré, G. *et al.* Hereditary spastic paraplegia type 43 (SPG43) is caused by mutation in *C19orf12*.
699 *Hum. Mutat.* **34**, 1357–1360 (2013).
- 700 41. Hartig, M. B. *et al.* Absence of an Orphan Mitochondrial Protein, C19orf12, Causes a Distinct Clinical
701 Subtype of Neurodegeneration with Brain Iron Accumulation. *Am. J. Hum. Genet.* **89**, 543–550 (2011).
- 702 42. Levi, S. & Tiranti, V. Neurodegeneration with Brain Iron Accumulation Disorders: Valuable Models
703 Aimed at Understanding the Pathogenesis of Iron Deposition. *Pharmaceuticals* **12**, 27 (2019).
- 704 43. Shao, C. *et al.* C19orf12 ablation causes ferroptosis in mitochondrial membrane protein-associated with

- 705 neurodegeneration. *Free Radic. Biol. Med.* **182**, 23–33 (2022).
- 706 44. Venco, P. *et al.* Mutations of C19orf12, coding for a transmembrane glycine zipper containing
707 mitochondrial protein, cause mis-localization of the protein, inability to respond to oxidative stress and
708 increased mitochondrial Ca²⁺. *Front. Genet.* **6**, 185 (2015).
- 709 45. Kotera, I., Iwasaki, T., Imamura, H., Noji, H. & Nagai, T. Reversible Dimerization of *Aequorea victoria*
710 Fluorescent Proteins Increases the Dynamic Range of FRET-Based Indicators. *ACS Chem. Biol.* **5**, 215–
711 222 (2010).
- 712 46. Bastian, F. B. *et al.* The Bgee suite: integrated curated expression atlas and comparative transcriptomics
713 in animals. *Nucleic Acids Res.* **49**, D831–D847 (2021).
- 714 47. Wieckowski, M. R., Giorgi, C., Lebiezinska, M., Duszynski, J. & Pinton, P. Isolation of mitochondria-
715 associated membranes and mitochondria from animal tissues and cells. *Nat. Protoc.* **4**, 1582–1590
716 (2009).
- 717 48. Brickley, K. & Stephenson, F. A. Trafficking Kinesin Protein (TRAK)-mediated Transport of
718 Mitochondria in Axons of Hippocampal Neurons. *J. Biol. Chem.* **286**, 18079–18092 (2011).
- 719 49. López-Doménech, G. *et al.* Miro proteins coordinate microtubule- and actin-dependent mitochondrial
720 transport and distribution. *EMBO J.* **37**, 321–336 (2018).
- 721 50. Wu, F. *et al.* Loss of mouse C19orf12 homolog disturbs tubular ER homeostasis and leads to
722 neuroaxonal dystrophy. *Acta Neuropathol. Commun.* **13**, 233 (2025).
- 723 51. Kim, D., Paggi, J. M., Park, C., Bennett, C. & Salzberg, S. L. Graph-based genome alignment and
724 genotyping with HISAT2 and HISAT-genotype. *Nat. Biotechnol.* **37**, 907–915 (2019).

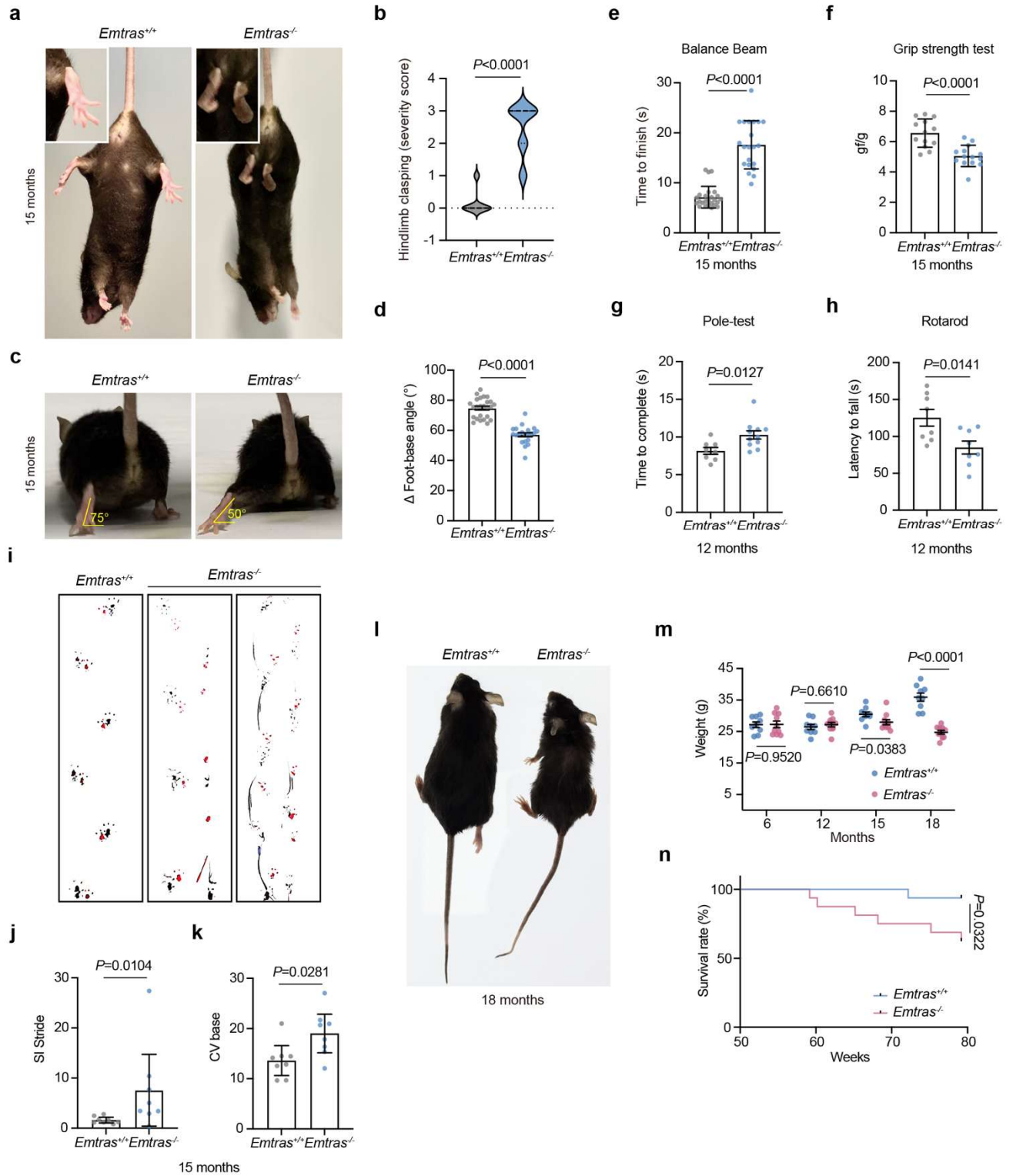


Fig. 1 | EMTRAS deficiency leads to progressive motor impairment and HSP-like pathology in mice

a, Representative images of 15-month-old *Emtras*^{+/+} and *Emtras*^{-/-} mice, showing hindlimb posture during tail suspension. Insets highlight hindlimb claspings.

b, Violin plot showing hindlimb claspings scores (scale 0-4) in *Emtras*^{+/+} ($n = 27$) and *Emtras*^{-/-} ($n = 25$) mice. Each dot represents one animal. The dashed line indicates a score of 0. Statistical significance was assessed by unpaired two-tailed t-test.

c, Representative images showing hindlimb splay angles during forward locomotion in *Emtras*^{+/+} and *Emtras*^{-/-} mice at 15 months of age.

d, Quantification of hindlimb splay angles during locomotion shown in **c**. Each dot represents one animal ($n = 25$ *Emtras*^{+/+} and 21 *Emtras*^{-/-} mice). Bars indicate mean \pm s.e.m. Statistical significance was assessed by unpaired two-tailed t-test.

e-h, Motor coordination and strength assessed by balance beam (**e**, $n = 25$ *Emtras*^{+/+}, 21 *Emtras*^{-/-}), grip strength (**f**, $n = 13$ *Emtras*^{+/+}, 14 *Emtras*^{-/-}), pole test (**g**, $n = 8$ *Emtras*^{+/+}, 11 *Emtras*^{-/-}), and rotarod assays (**h**, $n = 8$ *Emtras*^{+/+}, 8 *Emtras*^{-/-}) in *Emtras*^{+/+} and *Emtras*^{-/-} mice at 12 months of age. Each dot represents one animal. Bars indicate mean \pm s.e.m. Statistical significance was assessed by unpaired two-tailed t-test.

i-k, Representative gait traces (**i**) and quantification of gait parameters (**j**, **k**) including the stride symmetry index (**j**, SI stride) and step variability (**k**, CV base) in *Emtras*^{+/+} and *Emtras*^{-/-} mice. SI stride reflects left-right stride symmetry, with lower values indicating greater symmetry. CV base represents step-to-step variability and serves as a measure of gait stability. Each dot represents one animal ($n = 8$ per group). Bars indicate mean \pm s.e.m. Statistical significance was assessed by two-tailed Mann-Whitney test.

l, Representative images of *Emtras*^{+/+} and *Emtras*^{-/-} mice at 18 months of age.

m, Body weight measurements of *Emtras*^{+/+} and *Emtras*^{-/-} mice at the indicated ages. Each dot represents one animal ($n = 9$ *Emtras*^{+/+}, 11 *Emtras*^{-/-}). Bars indicate mean \pm s.e.m. Statistical significance was assessed by unpaired two-tailed t-test.

n, Kaplan-Meier survival curves of *Emtras*^{+/+} and *Emtras*^{-/-} mice ($n = 15$ *Emtras*^{+/+}, 17 *Emtras*^{-/-}). Statistical significance was assessed by the log-rank test.

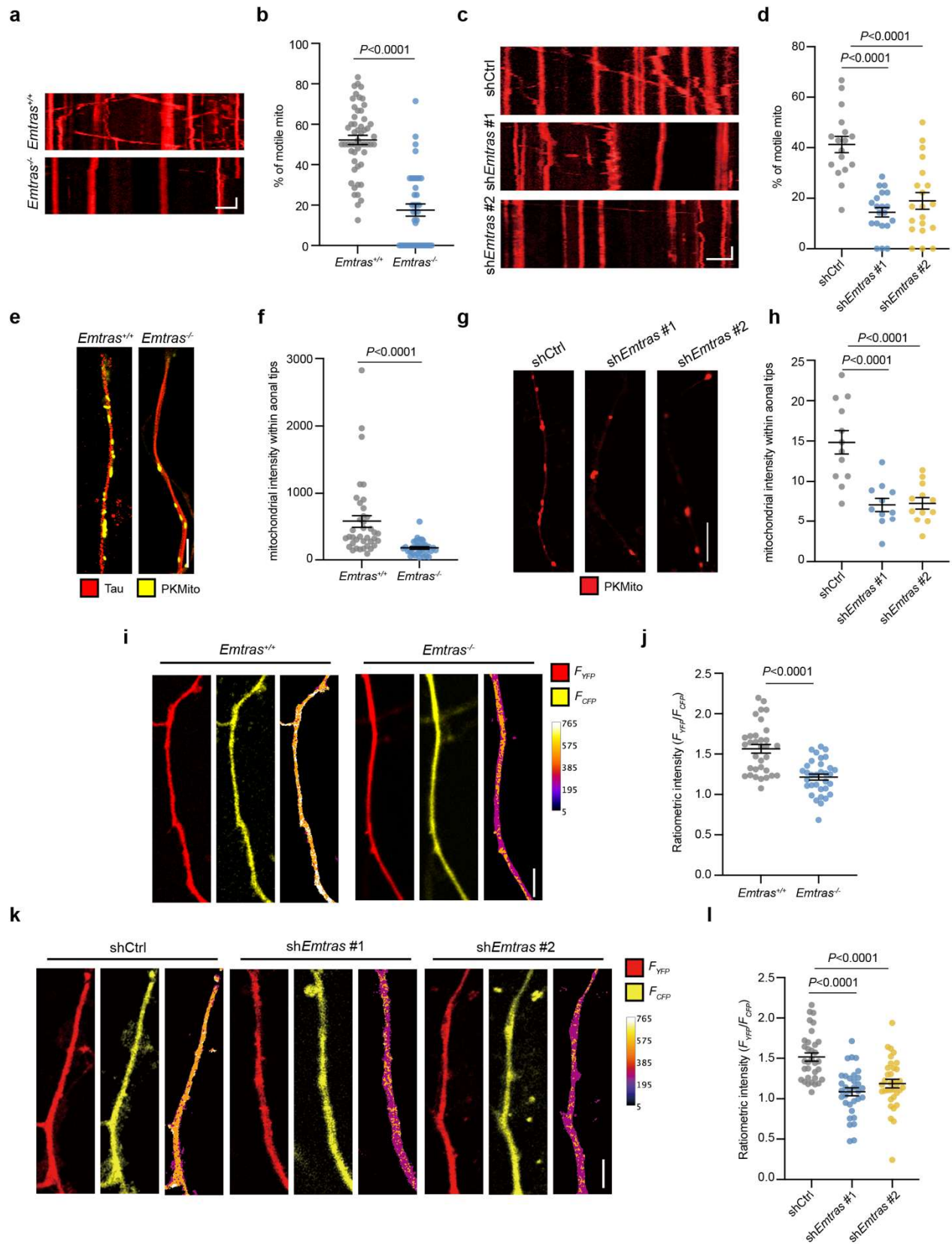


Fig. 2 | Loss of EMTRAS impairs axonal mitochondrial distribution, motility and function

a, Representative kymographs showing axonal mitochondrial movement in *Emtras*^{+/+} and *Emtras*^{-/-} neurons. Scale bars, 5 μ m (horizontal) and 1 min (vertical).

b, Quantification of the percentage of motile mitochondria in axons of *Emtras*^{+/+} ($n = 53$) and *Emtras*^{-/-} ($n = 38$) neurons. Each dot represents one axon. Horizontal bars indicate mean \pm s.e.m. Statistical significance was assessed by unpaired two-tailed t-test.

c, Representative kymographs showing axonal mitochondrial movement in neurons expressing shCtrl, sh*Emtras* #1 or sh*Emtras* #2. Scale bars, 5 μ m (horizontal) and 1 min (vertical).

d, Quantification of the percentage of motile mitochondria in axons under the indicated conditions in **c** ($n = 17$ shCtrl, 20 sh*Emtras* #1 and 20 sh*Emtras* #2). Each dot represents one axon. Horizontal bars indicate mean \pm s.e.m. Statistical significance was assessed by one-way ANOVA with multiple comparisons.

e, Representative images of axonal mitochondria labeled with PKMito in neurons derived from *Emtras*^{+/+} and *Emtras*^{-/-} genotypes. Tau staining marks axons.

f, Quantification of mitochondrial intensity within axonal tips in *Emtras*^{+/+} ($n = 38$) and *Emtras*^{-/-} ($n = 34$) neurons. Each dot represents one axon. Horizontal bars indicate mean \pm s.e.m. Statistical significance was assessed by unpaired two-tailed t-test.

g, Representative confocal images of axonal mitochondria labeled with PKMito (red) in neurons expressing shCtrl, sh*Emtras* #1 or sh*Emtras* #2. Scale bars, 5 μ m.

h, Quantification of mitochondrial intensity within axonal tips under the conditions shown in **g** ($n = 12$ shCtrl, 11 sh*Emtras* #1 and 12 sh*Emtras* #2). Each dot represents one axon. Horizontal bars indicate mean \pm s.e.m. Statistical significance was assessed by one-way ANOVA with multiple comparisons.

i, Representative images of axonal mitochondria expressing the ratiometric mitochondrial ATP sensor ATeam1.03, shown as F_{YFP} (red), F_{CFP} (yellow), and pseudocolor ratio images (F_{YFP}/F_{CFP}), in *Emtras*^{+/+} and *Emtras*^{-/-} neurons. Scale bars, 5 μ m.

j, Quantification of ratiometric mitochondrial ATP signal (F_{YFP}/F_{CFP}) reported by GoATeam1.03 in axons under the indicated conditions in **i** ($n = 33$ per group). Each dot represents one axon. Horizontal bars indicate mean \pm s.e.m. Statistical significance was assessed by one-way ANOVA with multiple comparisons.

i, Representative images of axonal mitochondria expressing the ratiometric mitochondrial ATP sensor ATeam1.03, shown as F_{YFP} (red), F_{CFP} (yellow), and pseudocolor ratio images (F_{YFP}/F_{CFP}), in neurons expressing shCtrl, sh*Emtras* #1 or sh*Emtras* #2. Scale bars, 5 μ m.

j, Quantification of ratiometric mitochondrial ATP signal (F_{YFP}/F_{CFP}) reported by the mitochondrial ATP sensor ATeam1.03 in axons of neurons expressing shCtrl ($n = 33$), sh*Emtras* #1 ($n = 33$) or sh*Emtras* #2 ($n = 34$). Each dot represents one axon. Horizontal bars indicate mean \pm s.e.m. Statistical significance was assessed by

unpaired two-tailed t-test.

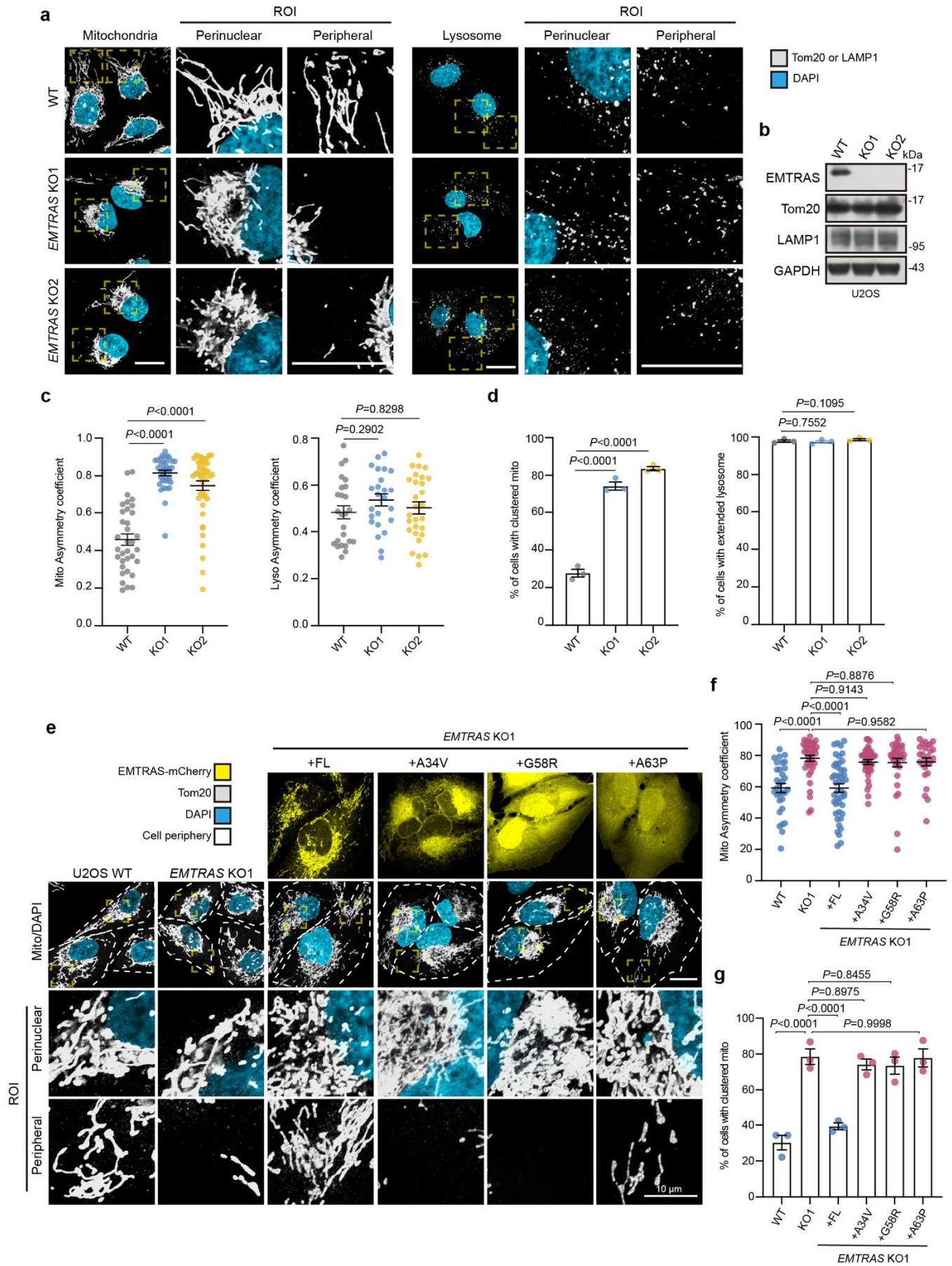


Fig. 3 | Loss of EMTRAS induces perinuclear clustering of mitochondria in U2OS cells

a, Representative confocal images of U2OS wild-type (WT) and two independent *EMTRAS* knockout (KO) clones stained for mitochondria (Tom20, grey) and lysosomes (LAMP1, grey). Nuclei were labeled with DAPI (blue). Box regions indicate ROIs. Scale bars, 20 μ m.

b, Immunoblot confirming loss of EMTRAS in two independent KO clones. Tom20 and LAMP1 were used as mitochondrial and lysosomal markers, respectively; GAPDH served as a loading control.

c, Quantification of mitochondrial (left, $n = 34, 37, 46$ from left to right) and lysosomal (right, $n = 25, 24, 28$ from left to right) asymmetry coefficients in WT and *EMTRAS* KO U2OS cells.

d, Quantification of the percentage of U2OS cells exhibiting perinuclear clustering of mitochondria (left) or lysosomes (right) following *EMTRAS* knockout. $n = 3$ experiments, with at least 150 cells counted per condition.

e, Representative confocal images of mitochondrial distribution in *EMTRAS* KO cells re-expressing mCherry-tagged WT or mutant EMTRAS (A34V, G58R and A63P). Mitochondria were labeled by Tom20 (grey) and nuclei by DAPI (Blue). Cell periphery is outlined by white dashed lines. Box regions indicate ROIs. Scale bars, 20 μ m.

f, g, Quantification of mitochondria asymmetry coefficient (**f**, $n = 31, 39, 45, 36, 33, 26$ from left to right) and percentage of cells with perinuclear mitochondrial clustering (**g**, $n = 3$ experiments, with at least 150 cells counted per condition) under the indicated conditions in **e**.

All quantitative data are shown as mean \pm s.e.m. In **c** and **f**, each dot represents one cell and statistical significance was assessed by one-way ANOVA with multiple comparisons. In **d** and **g**, each dot represents one biological replicate, the statistical significance was determined by Kruskal-Wallis test with multiple comparisons.

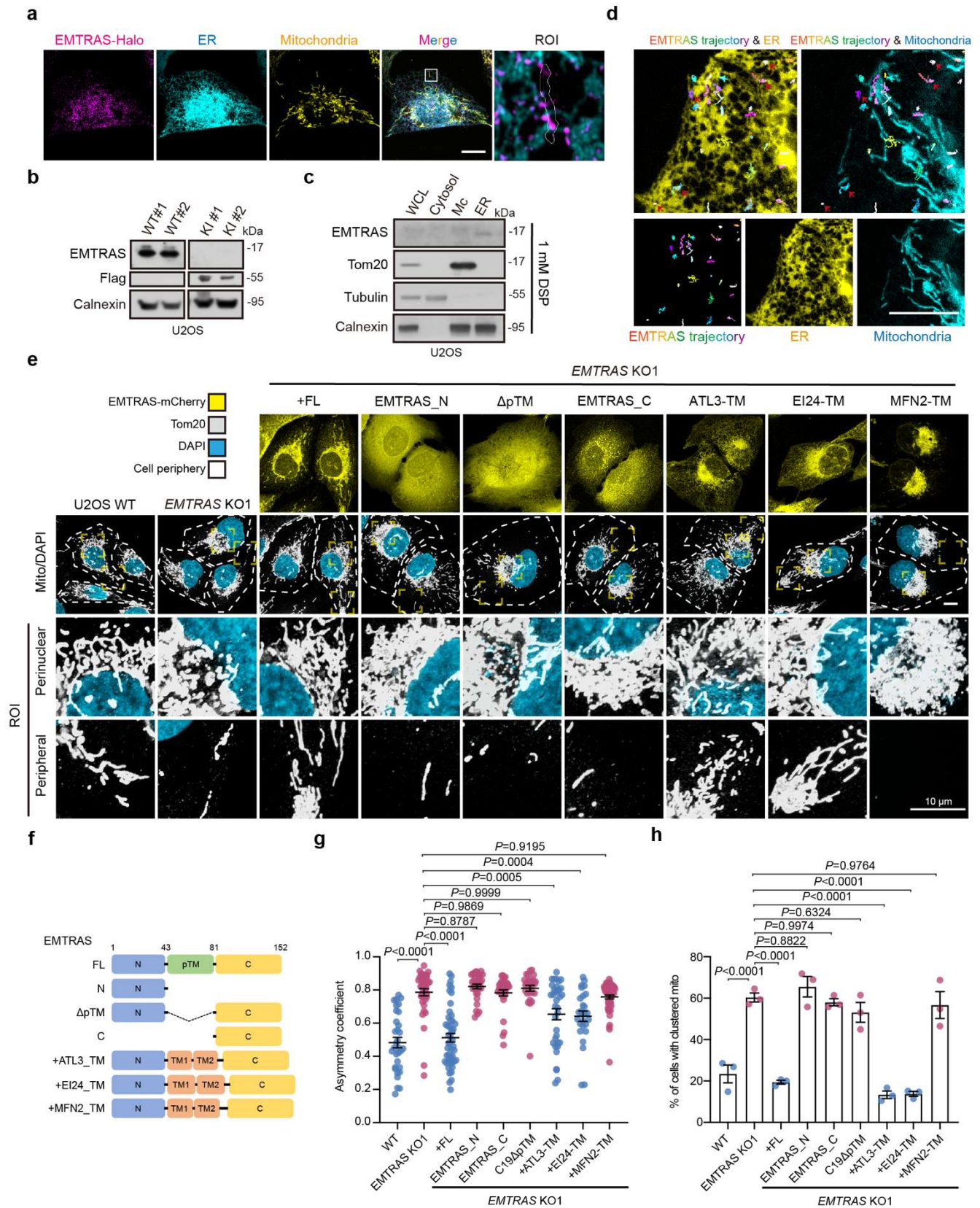


Fig. 4 | EMTRAS is a dynamic ER-anchored protein enriched at ER–mitochondria contact sites, and its ER localization is essential for regulating mitochondrial distribution

a, Representative confocal images of U2OS EMTRAS–Halo knock-in (KI) cells transiently expressing the ER marker Sec61 β (cyan) and stained for mitochondria (Tom20, yellow). The merged image shows EMTRAS localization relative to ER and mitochondria. Boxed regions indicate ROIs shown at higher magnification. Scale bars, 20 μ m.

b, Immunoblot confirmation of the *EMTRAS*-Halo knock-in (KI) allele in U2OS clones.

c, Subcellular fractionation of U2OS cells after chemical crosslinking followed by immunoblot analysis of whole-cell lysate (WCL), cytosol, crude mitochondria (Mc) and ER-enriched (ER) fractions. Tom20, Tubulin and Calnexin were used as mitochondrial, cytosolic and ER markers, respectively.

d, Single-molecule tracking of EMTRAS in U2OS *EMTRAS*–Halo KI cells transiently expressing Sec61 β (yellow) and labeled with the mitochondrial dye PKMito (cyan). Representative trajectories illustrate dynamic movement of EMTRAS relative to the ER and mitochondria. Red arrows indicate EMTRAS molecules moving along the ER network that do not overlap with mitochondria. Scale bar, 20 μ m.

e, Representative confocal images of mitochondrial distribution in *EMTRAS* KO cells re-expressing mCherry-tagged WT or the indicated truncation and transmembrane-domain chimeric constructs. Mitochondria were labeled with Tom20 (grey) and nuclei with DAPI (blue). Tubulin staining is shown as a cell morphology reference. Scale bar, 20 μ m.

f, Schematic representation of the EMTRAS domain deletion and chimeric constructs used for the rescue experiments in **e**. The native predicted transmembrane (pTM) domain of EMTRAS was deleted (Δ pTM) or replaced with ER-targeting TMs (from ATL3 or EI24) or a mitochondria-targeting TM (from MFN2).

g, Quantification of mitochondrial asymmetry coefficients under the indicated conditions in **e** ($n = 32, 40, 49, 32, 31, 29, 35, 27, 53$ from left to right). Each dot represents one cell; data are shown as mean \pm s.e.m. Statistical significance was assessed by one-way ANOVA with multiple comparisons.

h, Quantification of the percentage of cells exhibiting perinuclear clustering of mitochondria under the indicated conditions in **e** ($n = 3$ experiments, with at least 150 cells counted per condition). Each dot represents one biological replicate, the statistical significance was determined by Kruskal-Wallis test with multiple comparisons.

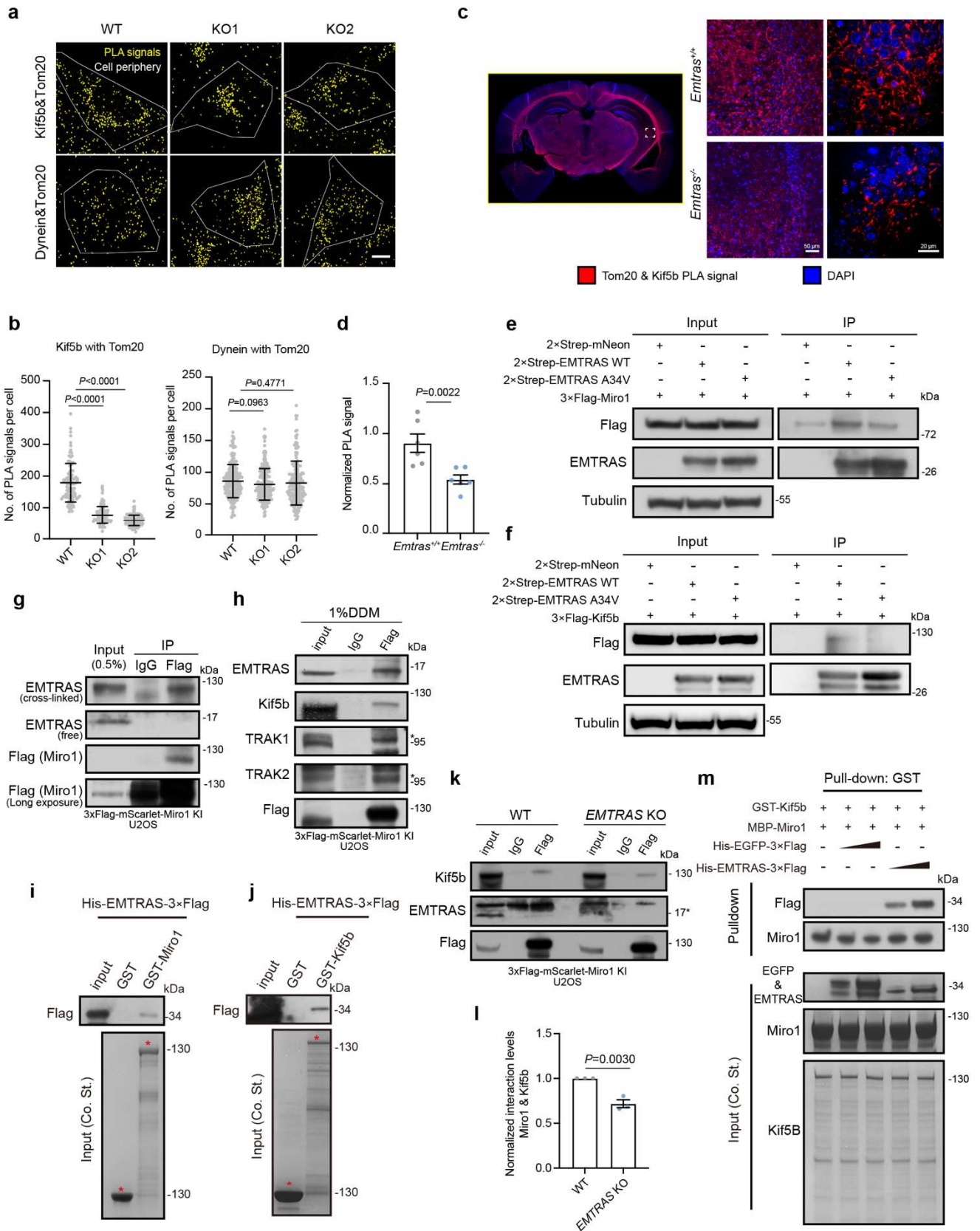


Fig. 5 | EMTRAS scaffolds the assembly of the Miro1-kinesin anterograde transport complex

a, Representative proximity ligation assay (PLA) images showing interactions between Kif5b and mitochondria (Kif5b–Tom20, top) or dynein and mitochondria (Dynein–Tom20, bottom) in U2OS WT and *EMTRAS* KO cells. PLA signals are shown in yellow; cell periphery is outlined. Scale bars, 10 μ m.

b, Quantification of the number of PLA signals per cell for Kif5b–Tom20 (left, $n = 99, 113, 112$ from left to right) and Dynein–Tom20 (right, $n = 217, 246, 168$ from left to right) interactions under the indicated conditions. Each dot represents one cell; horizontal bars indicate mean \pm s.e.m. Statistical significance was assessed by one-way ANOVA with multiple comparisons.

c, Representative images of brain sections from *Emtras*^{+/+} and *Emtras*^{-/-} mice stained for proximity ligation assay (PLA) signals detecting Tom20–Kif5b interactions (red) and nuclei (DAPI, blue). Dashed boxes indicate regions shown at higher magnification. Scale bars, 50 μ m (left), and 20 μ m (right).

d, Quantification of normalized PLA signal intensity in brain sections shown in **a** ($n = 6$ per group). Each dot represents one animal. Bars indicate mean \pm s.e.m. Statistical significance was assessed by unpaired two-tailed t-test.

e-f, Co-immunoprecipitation assays in 293T cells showing interactions between EMTRAS and mitochondrial transport proteins. 2 \times Strep-tagged EMTRAS (WT or A34V) was co-expressed with either 3 \times Flag–Miro1 (**e**) or 3 \times Flag–Kif5b (**f**). Input and immunoprecipitated samples were analyzed by immunoblotting with the indicated antibodies.

g, Immunoprecipitation of endogenous EMTRAS from U2OS cells harboring a 3 \times Flag–mScarlet–Miro1 knock-in, performed under DSP chemical crosslinking conditions. Input and immunoprecipitated samples were analyzed by immunoblotting to detect crosslinked and non-crosslinked forms of EMTRAS and associated proteins, as indicated.

h, Immunoprecipitation of 3 \times Flag–mScarlet–Miro1 U2OS KI cells performed in the presence of 1% n-dodecyl- β -D-maltoside (DDM), followed by immunoblot analysis of co-precipitating EMTRAS and mitochondrial transport proteins.

i, j, In vitro GST pull-down assays using purified His–EMTRAS–3 \times Flag and GST-tagged Miro1 (**i**) or Kif5b (**j**). Input and bound fractions were analyzed by immunoblotting for Flag. Coomassie blue staining indicates the loading of purified proteins.

k Immunoprecipitation of 3 \times Flag–mScarlet–Miro1 U2OS KI cells in which EMTRAS was subsequently deleted, followed by immunoblot analysis of co-precipitating Miro1 and Kif5b. Input, IgG and Flag immunoprecipitations are shown.

l, Quantification of normalized interaction levels between Miro1 and Kif5b in WT and *EMTRAS* KO cells, based on data in **i** ($n = 3$ experiments). Data are shown as mean \pm s.e.m.; statistical significance was assessed by unpaired two-tailed t-test.

m, Competitive in vitro GST pull-down assays using GST–Kif5b and MBP–Miro1 in the presence of increasing amounts of purified His–EMTRAS–3×Flag or His–EGFP–3×Flag as a control. Bound fractions were analyzed by immunoblotting for Flag and Miro1. Coomassie blue staining indicates protein loading.

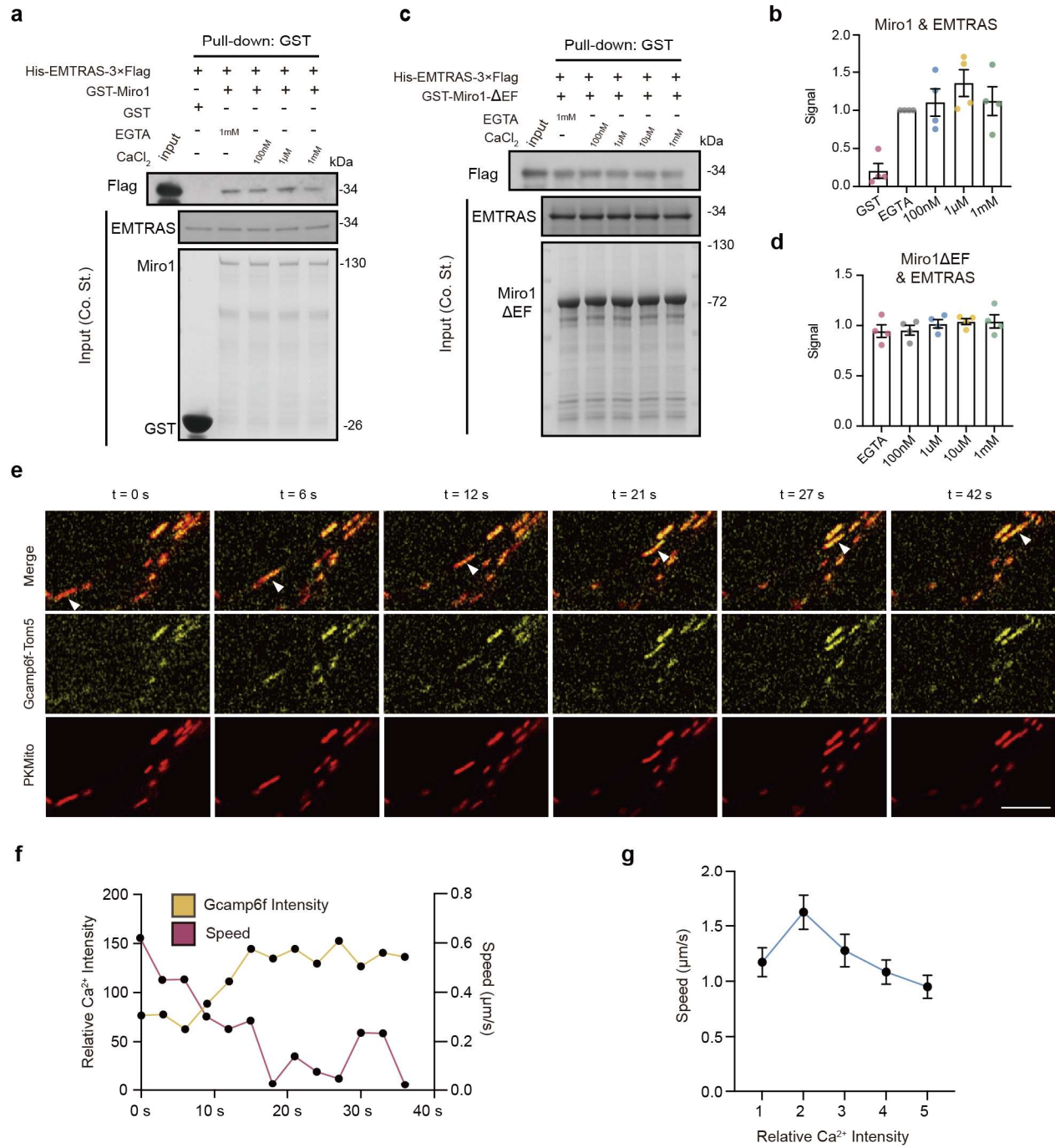


Fig. 6 | Calcium modulates the assembly of the EMTRAS-Miro1 transport machinery

a, c, In vitro GST pull-down assays examining the interaction between purified His-EMTRAS-3×Flag and GST-Miro1 (**a**) or GST-Miro1-ΔEF-hand (**c**) in the presence of the indicated concentrations of CaCl₂ or EGTA. Input and bound fractions were analyzed by immunoblotting for Flag. Coomassie blue staining indicates protein loading.

b, d, Quantification of EMTRAS-Miro1 (**b**, $n = 4$ experiments) and EMTRAS-Miro1-ΔEF-hand (**d**, $n = 3$ experiments) interaction signals from pull-down assays shown in **a, c**. Data are shown as mean \pm s.e.m. from independent experiments.

e, Representative time-lapse images of axonal mitochondria labeled with PKMito (red) and Ca²⁺ signals reported by transiently expressed GCaMP6f-Tom5 (yellow) in living cells. Arrowheads indicate a representative mitochondrion exhibiting a characteristic transient Ca²⁺ signal over time. Scale bars, 20 μ m.

f, Representative traces showing temporal changes in relative mitochondrial Ca²⁺ intensity (GCaMP6f-Tom5) and mitochondrial movement speed from the individual mitochondrion indicated by arrowheads in **d**.

g, Quantification of mitochondrial movement speed grouped by relative surface calcium intensity levels. $n = 52$ per group. Data are shown as mean \pm s.e.m. in every group.

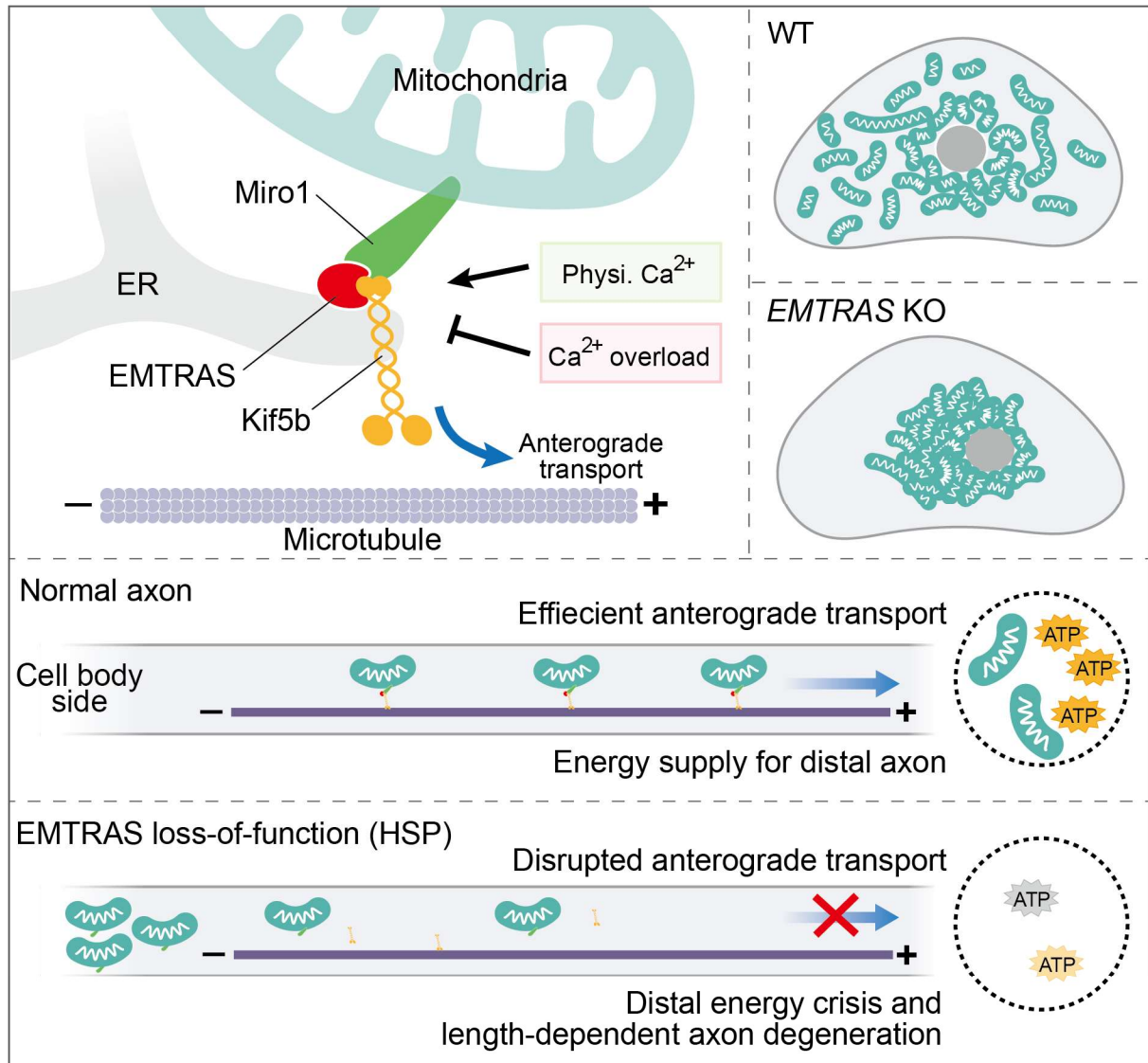


Fig. 7 | Proposed model: EMTRAS acts as an ER-anchored scaffold to orchestrate mitochondrial transport

EMTRAS molecular mechanism at ER-Mitochondria contact site (Top left). Under physiological conditions, EMTRAS is dynamically anchored to the ER membrane at ER-mitochondria contact sites. It functions as a specialized scaffold that bridges the ER to mitochondria, promoting the assembly of mitochondrial transport complex formed by mitochondrial outer membrane protein Miro1 and the anterograde motor Kinesin-1 (Kif5b). Importantly, this assembly is modulated by local Ca^{2+} levels, being optimal at physiological concentrations found at contact sites but significantly weakened under calcium overload.

Cellular regulation of mitochondrial distribution (Top right). In WT cells (top), EMTRAS promotes the peripheral distribution of mitochondria. In the absence of EMTRAS (middle), the outward transport machinery is compromised, leading to severe mitochondrial perinuclear clustering.

Neuronal consequences and HSP pathology (Bottom): In physiological conditions, EMTRAS-mediated transport ensures the robust delivery of mitochondria to distal axonal terminals, maintaining high local ATP levels required for synaptic homeostasis. In pathological conditions, the failure of EMTRAS-dependent transport leads to a progressive depletion of mitochondria at the distal axon. This results in a local energy crisis (low ATP) at synaptic terminals, driving the "dying-back" length-dependent axonopathy characteristic of Hereditary Spastic Paraplegia (HSP).